Mitigation of Turbulent Noise Sources by Riblets

Chioma Muhammad, Tze Pei Chong*

[a]*Department of Mechanical and Aerospace Engineering, Brunel University London, Uxbridge, UB8 3PH, United Kingdom*

Abstract

A feasibility study is presented on the application of riblets to suppress turbulent pressure sources leading to a reduction in the generation of aerofoil self-noise. It is shown that riblets can reduce skin friction as well as the turbulence intensity inside the boundary layer. In addition, near-wall turbulence structures were found to be dissipated quite rapidly when crossing the riblets surface. It is found that riblets (1) slightly reduce the wall fluctuating pressure power spectral density level at the low and high frequency ranges, but cause an increase at the mid frequency range, and (2) reduce the lateral turbulence coherence length scale across a large frequency range. As a result, riblets have the potential to reduce trailing edge noise at the low and high frequency regions. The fundamental mechanism by which riblets reduce the turbulent intensity level inside the boundary layer is investigated by studying the spatio-temporal evolution of turbulent spots, which are commonly regarded as the building blocks of a turbulent boundary layer. In this paper two mechanisms are proposed. First, the enhanced momentum achieved at the becalmed region of each turbulent spot will lead to a reduction in the overall turbulence intensity obtained when turbulent spots merge downstream. Second, the internal turbulence level at the rear part of a turbulent spot can be reduced directly by an enhanced re-laminarisation effect.

Keywords: riblets, wall pressure fluctuation, trailing edge noise

*Corresponding author

Email address: t.p.chong@brunel.ac.uk (Tze Pei Chong)

1. Introduction

The current engineering landscape is so multifaceted that the environmental and societal responsibilities can no longer be treated just as an afterthought. The measurement of performance for an industrial blade cannot be solely based on the generated aerodynamic forces. The wind turbine industry, for example, is constantly seeking novel technology to create new industrial aerofoil fan blade systems that are both aerodynamically efficient and aeroacoustically quiet.

One of the major noise sources for an aerofoil is the trailing edge self-noise [1]. The descriptive wording of *self-noise* stems from the fact that the far field radiation originates from the hydrodynamic field near the trailing edge. However, it is also important to note that the amplitude of the radiated sound and its spectral characteristics are dependent on the state of the boundary layer, which is governed by several external factors such as the surface roughness, Reynolds number, pressure gradient and so on. One type of self-noise that is especially relevant to the industrial applications is when the boundary layer has undergone a complete transition to fully turbulent at the trailing edge. In this scenario a cascade of turbulent length scale eddies are scattered into a broad frequency band of acoustic disturbances into the far field.

Source targeting can be an effective principle to reduce the radiated turbulent broadband noise level. More specifically, one can aim to manipulate, alter or inhibit the growth mechanisms of the turbulent boundary layer. Mounting finlets near the trailing edge has been shown to significantly alter the turbulent boundary layer structure and reduce the radiated noise level [2, 3]. Attaching a serration at the trailing edge represents another proven method for self-noise reduction. In addition to the acoustical destructive interference mechanism [4, 5], a serrated trailing edge can also trigger additional streamwise structures to interfere with the turbulent boundary layer, and slow down the propagation rate of the eddies near the oblique edges [6, 7]. This represents a source targeting approach, which may co-exist with the acoustical destructive interference mechanism to make a serrated trailing edge an effective passive device for the reduction of self-noise radiation. Acoustical destructive interference can also be enforced in a trailing edge with a structured porous surface. For example, Scholz *et al.* [8] demonstrated that placing a single row porous array at the rear part of aerofoil can force the turbulent eddies to scatter twice: first at the spanwise porous row,

and second at the trailing edge. The phase difference between the scattering locations thus gives rise to a frequency tuning capability for the noise reduction. However, the dominant mechanism of noise reduction by porous trailing edge is believed to be the source targeting, which entails a manipulation of the turbulent boundary layer's fundamental hairpin structures, turbulent re-generation mechanisms, slip velocity, and so on. For example, a turbulent boundary layer passing over a porous surface with a strong wall-normal permeability can lift up the near wall low-speed streaks [9], thereby displacing the turbulence away from the wall surface and reducing the near wall turbulence source strength. Indeed, making the aerofoil trailing edge porous has been shown to produce low-level of self-noise radiation [10]. A recent review article that contains some discussions of porous surface to the aerofoil turbulent self-noise mitigation can be found in Lee *et al.* [11].

An aerofoil with a sharp trailing edge generally represents a streamlined body with a low-drag characteristic at the pre-stall condition. The design feature of aerofoil will be destroyed by the addition of finlets, serrations, or porous treatment to the trailing edge where increases of drag coefficients have generally been observed. Thus, a research question worth exploring is whether there exists a passive device that can simultaneously reduce the drag and noise.

From the first observation of the fast swimming capability of sharks to the discovery of dermal denticles on their skin, the use of *riblets* to reduce skin friction on engineering surface is one of the most researched topics in the fluid mechanics community. The riblets can be configured in different forms, such as the v-groove (or sawtooth) [12], trapezoidal-groove [13], and scalloped [14]. Recently, the development of riblets on flow control also focuses on the enhancement of strong secondary flow to achieve spanwise modulation of the boundary layer, such as the convergent-divergent riblets [15]. Each of the configurations mentioned above has achieved various degree of success in realising the drag reduction potential. However, there seems to be conflicting findings on some of the mechanisms exerted by the riblets to the turbulent boundary layer structures. For example, some have found that the bursting frequency of the low-speed streak remains unchanged under riblets [12, 16], but others observed that the weakened near wall burst is one of the main reasons for the reduced turbulence production [17, 18].

If the riblets' mean protuberance height is h, and the mean spanwise spacing between the protuberances is S, then plotting the skin friction coefficient against either the hu_τ/ν or Su_τ/ν will result in a non-symmetric parabolic

characteristic (see for example [19]). Here u_τ is the friction velocity, and ν is the kinematic viscosity. This means that there exists a small range of optimal riblets geometry that is the most effective in the skin friction reduction. A riblets geometry that is below the optimal range might still be able to produce low-level of skin friction reduction. However, if a riblets geometry is too large, it will be seen as a surface roughness where an opposite effect of drag increase will happen. This highlights that the extent of manipulation to the turbulent structures by riblets is extremely sensitive to its geometry under a specific flow condition.

When the riblets geometry is optimised, the low-speed streaks in the sublayer can be constrained in the trough between the riblets protuberances, thereby restricting the spanwise meandering of the wall vortices in their turbulence self-generating process. Many studies have also reported a reduction of the boundary layer turbulence intensity level on the riblets surface. These observations suggest that the riblets have a potential to produce a source targeting execution to achieve self-noise reduction. Unlike the previous candidates (finlets, serrations and porous), riblets have a potential to achieve reductions in drag and noise simultaneously.

This work represents a feasibility study to investigate the potential of riblets to reduce the turbulent pressure sources that are important for aerofoil self-noise radiation. To the best knowledge of the authors, the change in the turbulence structures by riblets has not been studied much from the perspective of the wall pressure fluctuation field. Furthermore, it still remains relatively scarce in the literature that describes the turbulence spectral characteristics produced by riblets. This paper aims to fill this gap, and tries to shed some lights on riblets for their potential to be a trailing edge self-noise reduction device. A flat plate system, which has a semi-hollow section to allow the interchange between a baseline (smooth surface) test plate and a riblets test plate, is employed here. This study also utilises a special boundary layer tripping technique that can result in a controlled and periodic generation of turbulent spots in an otherwise laminar boundary layer. The rationale is that, being the *building block* of a fully-developed turbulent boundary layer, the turbulent spots can be studied in both the spatio and temporal domains to facilitate a fundamental investigation of the dynamical changes in the momentum and turbulence characteristics when the turbulent spots propagate over the riblets surface.

2. Experimental Setup, Measurement and Analysis Techniques

The experiments were conducted in an open circuit, suction type wind tunnel where the axial fan is driven by a 7.5 kW motor capable of achieving velocity up to 35 $\mathrm{m\,s^{-1}}$ inside the 0.5×0.5 m working section. The walls are constructed by Perspex to allow optical access. The mean turbulence intensity of the flow is measured to be less than 0.5%.

2.1. Design of a flat plate system

As shown in Figure 1, a flat plate that contains a recess in the middle section for interchangeable test plates was designed and built in-house. The coordinate system used in this study is also shown in the figure, where x, y and z denote the streamwise, wall-normal and spanwise directions, respectively. In the figure, there is a removal strip located at $x = 175$ mm, where $x = 0$ refers to the leading edge of the flat plate. This strip houses nine VISATON K23 $(8\Omega, 1W)$ loudspeakers across the spanwise direction, which are used to generate turbulent spots through a pinhole of 1 mm deep and 0.4 mm in diameter. The loudspeakers are wired in series, which allows all nine loudspeakers to be triggered simultaneously. The centre speaker (defined as $z = 0$) is specially wired in a configuration that allows it to be used on its

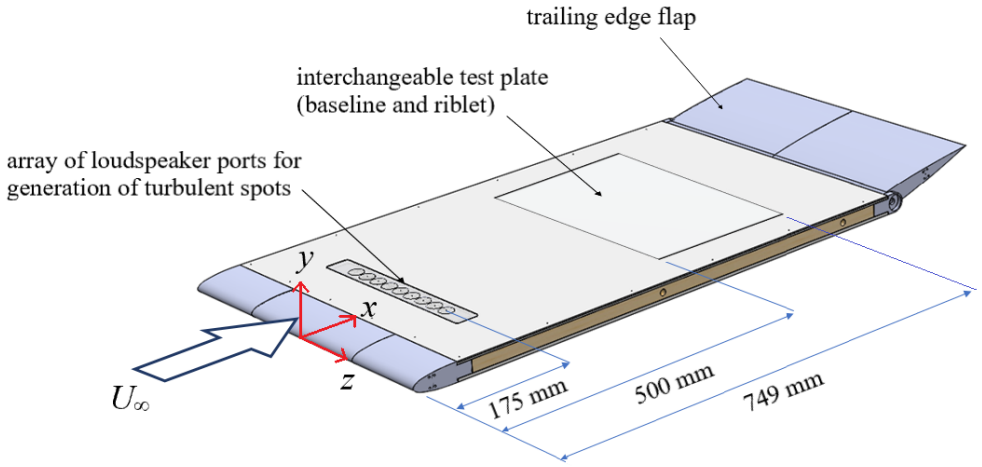

Figure 1: Schematic showing the flat plate model used in the current study. The coordinate system is also shown. Drawing is not to scale.

x (mm)	z (mm)
625 {*625*}	0, 2.0, 4.2, 6.6, 9.2, 12.0, 15.0, 18.2 {*0, 1.9, 4.5, 6.4, 9.0, 12.2, 14.7, 17.9*}
627 {*627*}	0 {*0*}
634 {*634*}	0 {*0*}
645 {*645*}	0, 2.0, 4.2, 6.6, 9.2, 12.0, 15.0, 18.2 {*0, 1.9, 4.5, 6.4, 9.0, 12.2, 14.7, 17.9*}
655 {*655*}	0 {*0*}
665 {*665*}	0, 2.0, 4.2, 6.6, 9.2, 12.0, 15.0, 18.2 {*0, 1.9, 4.5, 6.4, 9.0, 12.2, 14.7, 17.9*}
685 {*685*}	0 {*0*}
725 {*725*}	0, 2.0, 4.2, 6.6, 9.2, 12.0, 15.0, 18.2 {*0, 1.9, 4.5, 6.4, 9.0, 12.2, 14.7, 17.9*}

Table 1: Location of the streamwise and spanwise pressure taps for the wall pressure fluctuation measurements. The values in *italic* fonts inside the braces correspond to the riblets plate. Note that $z = 0$ represents the mid-span of the flat plate system.

own. In this study, only the centre loudspeaker is used to generate turbulent spots. Note that in the experiment when the centre loudspeaker is used to generate the turbulent spots, the boundary layer on the flat plate surface will be laminar. A trailing edge flap is used to control the front stagnation point to ensure a smooth boundary layer development on the upper flow surface, which is essential for the generation of turbulent spots [20]. When a fully developed two-dimensional turbulent boundary layer is required, a zig-zag type turbulator will be placed at the same location as the loudspeaker strip, $x = 175$ mm, to serve as a passive device to artificially trip the boundary layer.

For the test plate system, there is a recess between $500 \leq x \leq 749$ mm to house either a baseline, smooth surface test plate, or riblets surface test plate. Both test plates have the same overall length. For the baseline test plate, it has a smooth aluminium finish enabled by a 3-axis CNC machine. The plate consists of arrays of streamwise and spanwise distributed pressure tap holes

of 0.4 mm diameter for the measurement of the wall pressure fluctuations. Table 1 summarises the locations of these pressure taps. Note that not all of them are used in the measurement. For the remainder of this paper, $x = 625$ mm is treated as the reference measurement location, and is represented by X_{ref}.

2.2. Design of the riblets test plate

For the riblets test plate, the manufacturing process is understandably more complex. Some methods have been proven successful to manufacture riblets surface to various degree of success, including etching [21], laser machining [22], grinding [23], micro-moulding [24] and 3D printing by Wen *et al.* [25], who successfully employ multi material 3D printing system to print a sheet of shark dermal denticles. In the past, we have successfully performed the fly cutting method from a milling machine to produce a sub-scale serrated semi-circular riblets surface that can achieve up to 7% drag reduction [26]. However, the manufacturing process is quite complicated and time consuming. In the current study, we adopted the Stereolithography Apparatus (SLA) 3D printing technique to manufacture the riblets test plate, which has proven to be more straightforward to manufacture, and yet it can still achieve the required geometrical accuracy.

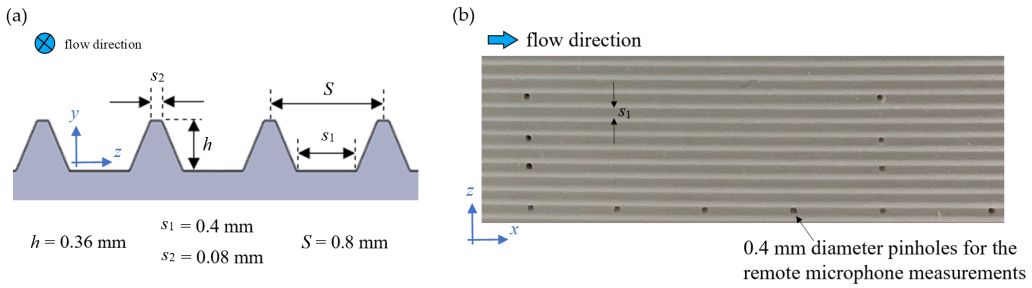

Figure 2: (a) Schematic (front view) illustrating the riblets geometry, and (b) photograph (plan view) showing a zoomed-in view ($\sim 29.0\,\text{mm} \times 9.2$ mm) of the riblets test plate used in the current study.

The riblets shape is chosen as a simple longitudinal sawtooth (triangular) shape, where some prototypes have been successfully printed. However, it became apparent that drilling pressure taps into the sawtooth riblets plate will cause the pressure taps to compromise the integrity and consistency of the surface, as well as to fall in different vertical locations of the individual

riblets. The latter scenario is especially crucial as it could compromise the overall accuracy of the wall fluctuating pressure measurements. To mitigate this, it is decided to create a flat surface between each protuberance, thus resembling a groove, when viewed in the $y-z$ plane. A schematic illustrating the riblets geometrical drawing is shown in Figure 2a, where a photograph taken from the plan view of the riblets test plate can be found in Figure 2b. In this study, only one riblets geometry is investigated.

In the figure, this particular riblets geometry can be described by h, s_1, s_2 and S. The s_1 is pre-determined as 0.4 mm to correspond to the pressure tap hole diameter. The s_2, which is ideally $\rightarrow 0$, is estimated to be 0.08 mm, which is equivalent to the laser beam diameter. S is a function of s_1 and s_2. Now, the decision on the value of h must be based on the turbulent boundary layer length scale. In the current study, the range of freestream velocity U_∞ over the flat plate surface is set at between 10 and 15 $\mathrm{m\,s^{-1}}$. Since the riblets test plate location has already been pre-fixed (Figure 1), the $1/7^{th}$ power law can be utilised to predict the skin friction coefficients, as well as the friction velocity u_τ during the design phase. The latter can be used to provide a non-dimensional riblets height hu_τ/ν. This non-dimensional quantity can then be compared against the $y^+ (= yu_\tau/\nu)$ in the law of the wall, which will provide information about the relative height of the riblets in the context of the turbulent boundary layer. In addition, the spanwise spacing can also be expressed in Su_τ/ν, which will provide information about the relative spanwise spacing between the riblets protuberances and the gap separating the adjacent low speed streaks for a coherent structure ($\sim 100z^+$).

After the riblets test plate has been manufactured, it is then installed onto the flat plate system as described in Figure 1, where boundary layer measurements were conducted to determine the u_τ, which will enable the quantification of the hu_τ/ν and Su_τ/ν at $U_\infty = 10, 12$ and 15 $\mathrm{m\,s^{-1}}$. Note that U_∞ is the freestream velocity. From the measurements, the riblets achieve $hu_\tau/\nu = 12.2, 14.3$ and 17.4 at $U_\infty = 10, 12$ and 15 $\mathrm{m\,s^{-1}}$, respectively. Therefore, the riblets are expected to fall within the buffer layer. For the spanwise spacing, Su_τ/ν equals to 27.1, 31.9 and 38.7 at $U_\infty = 10, 12$ and 15 $\mathrm{m\,s^{-1}}$, respectively. This suggests that, despite the application of spanwise offset to each of the riblets protuberance (s_1), it is still significantly smaller than the mean spanwise spacing between adjacent low-speed streaks of the coherent structures. Therefore, the riblets used in the current study are expected to be effective in the manipulation of the turbulent boundary layer. Finally, the distribution of the pressure tabs for the riblets plate can also be

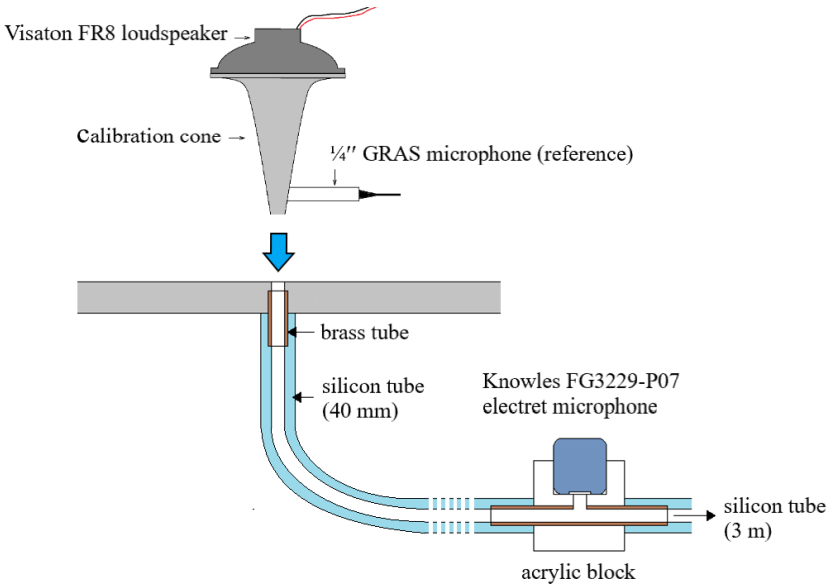

Figure 3: The remote microphone configuration (cross section view), including the calibration system.

found in Table 1. Note that the spanwise distribution of the pressures tab for the riblets test plate can be slightly different compared to the baseline, smooth test plate counterpart. This is due to the adjustment of the pressure tab to ensure that it is located within the s_1 of each groove. Nevertheless, the difference is very small ($\leq$ 0.3 mm), thus can be treated as negligible.

2.3. Instrumentation

The Knowles FG3229-P07 electret microphones, which are circular (2.57 mm diameter) with a sensing diameter of 0.8 mm, have been used in the wall pressure fluctuation measurements. As shown in Figure 3, the microphone is mounted remotely underneath the wall surface with an acrylic holder. It is connected to the wall surface via a 40 mm silicone tube. The same type of silicone tube of about 3 m long is connected to the other end of the acrylic holder, which will come out from the working section of the wind tunnel. The use of a long tube at the other end is to ensure that the acoustic waves travelling inside the remote microphone system does not encounter a sudden termination that will result in the backward reflection.

A Visaton FR8 10W full range speaker is used to calibrate each of the

remote microphone *in-situ*. It is attached to a cone that is designed to direct the sound pressure waves from a larger area to the other end of a smaller area. A similar calibration method was used by both Gruber [27] and Sagrado [28]. In this method, a $\frac{1}{4}''$ GRAS reference microphone with a known frequency response is embedded in the wall of the cone near the surface as shown in Figure 3. This allows the signal of the remote microphone and reference microphone to be measured simultaneously, thereby allowing us to determine the phase function of each remote microphone. During the experiment, the raw data from each remote microphone is sampled at a rate of 40 kHz for 15 seconds, which amounts to 600,000 samples. The data acquisition system has a 16-bit resolution and each sampling channel has a built-in anti-aliasing filter.

The flow velocity fluctuation is measured by a miniature, single hot wire (Dantec 55P11), which consists a 1.25 mm long, 5 μm diameter tungsten sensing wire. Operated by a constant temperature anemometer, the overheat ratio of the hot wire is set to 1.8, which will facilitate an operating temperature of the hot wire to be approximately 300°C. The hot wire is attached to a three axis traverse system, in which the step motors are capable of achieving very fine movement of 0.01 mm. Such a high spatial resolution in the traverse is suitable for the boundary layer measurement. The analogue-to-digital (A/D) card used in the hot wire acquisition has an 12-bit resolution. The data sampling rate is set at 20 kHz for 13 seconds for the tripped turbulent boundary layer (results presented in Section 3.1). The sampling time increases to 26 seconds for the turbulent spot case (results presented in Section 3.2). The doubling of sampling time is to ensure that each measurement point contains adequate number of individual turbulent spot signatures (approximately 80) to achieve an acceptable level of convergence for the ensemble averaging. In both the passively-tripped and actively-triggered boundary layer cases, a low-pass filter of 10 kHz is utilised in the data acquisition to ensure that the sampled signal is inside the Nyquist frequency and is not contaminated by aliasing. Temperature correction of the sampled hot wire signals is performed during the post-analysis.

Calibrated by a feeler gauge, the nearest height above the surface measured by the hot wire probe is approximately 0.15 mm. For the baseline test plate, the no-slip condition determines that the velocity should remain nil at the wall surface, where $u = 0$ at $y = 0$. This can be considered as the *origin*. For the riblets test plate, the point at which the turbulent boundary layer begins from the surface is less straightforwardly defined. Due to the

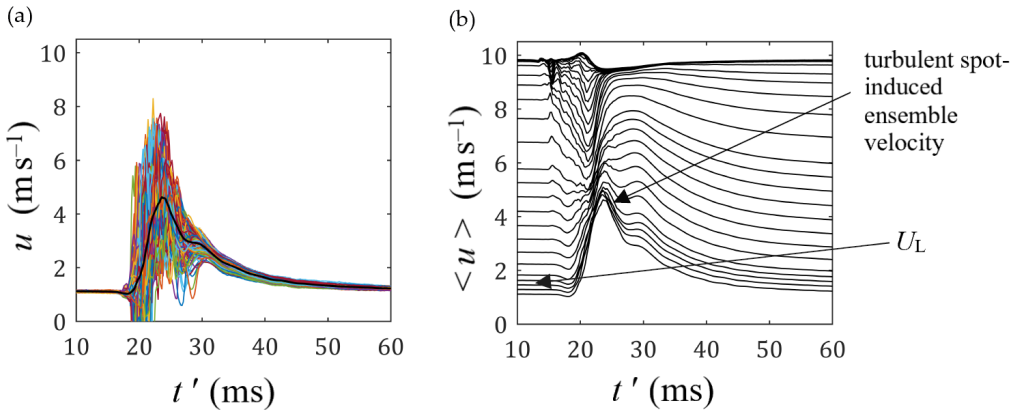

Figure 4: (a) An ensemble of velocity signals (colour lines) produced by 341 turbulent spots. The black solid line is the ensemble phase-averaged velocity $\langle u \rangle$, and (b) ensemble phase-averaged velocity signatures for a boundary layer, where each line represents the velocity measurements taken at different y locations from the wall surface. This example is taken from Chong and Juknevicius [30].

physical size of the hot wire probe, it is unable to reach the lowest part of the riblets surface, i.e. the groove between each riblets protuberance, and measure the local velocity accurately. In other words, the nearest y location that a hot wire probe can reach is above the riblets protuberance. This presents a dilemma of defining the origin pertaining to the riblets, where $y = 0$ could either be at the groove (i.e. the same as the baseline test plate), or at the surface of the riblets protuberance, or at a particular vertical distance between them. In the current study, a concept of the *virtual origin* is used instead. As reported by Bechert and Bartenwerfer [29], there is no universal definition of a virtual origin location because it is dependent on the riblets geometry h, and S. The determination of the virtual origin in the current works follows the method used by Lee and Lee [14], which is to match the non-dimensional mean streamwise velocity profiles between the baseline and riblets. Essentially, this method assumes that the $0.99U_\infty$ for both the baseline and riblets cases will occur at the same y location. To fulfil this condition, the boundary layer profile for the riblets may need to be shifted vertically. In this study, the virtual origin for the riblets is found to locate at around $0.66h$ below the riblets protuberance. This empirical value will be adopted throughout this study.

2.4. Generation of turbulent spots

Finally, some information about the generation of the turbulent spots, as well as their analysis methods, are discussed here. Referring to Figure 1, the turbulent spots are created artificially in an otherwise laminar boundary layer by injecting puffs of air through an 0.5 mm diameter orifice at $x = 175$ mm. Such turbulent spot generation method has been employed previously in [31, 32, 33] and others. The small air jet is generated by driving the miniature loudspeaker at the middle of the strip, i.e. $z = 0$. A Teledyne T3AFG10 function generator is used to generate the square wave pulse signals with a 1 ms pulse width at a frequency of 3 Hz. This particular spot generation frequency is confirmed as the ideal value to ensure that interaction between individual spot does not occur at all the measurement points, and at the same time not resulting in excessive overall sampling time required. The data analysis of the turbulent spot in this paper relies heavily on the ensemble averaging technique. To perform the ensemble averaging successfully, the rising edge of each input pulse signal can be set as the time of origin ($t' = 0$ ms) of an individual spot event. This allows the generation of an ensemble of velocity fluctuations, which is shown in Figure 4a from data obtained elsewhere [30] as an example. The ensemble is then averaged to obtain the mean velocity time signature $\langle u(x, y, t')\rangle$, which is represented by the thick black line in the figure. Typical mean velocity signatures at various y locations measured across a boundary layer is shown in Figure 4b. The velocity perturbation caused by an ensemble-averaged turbulent spot is given by:

$$\tilde{u}(x, y, t') = \frac{\langle u(x, y, t')\rangle - U_{\mathrm{L}}(x, y)}{U_{\infty}(x)}, \tag{1}$$

where $U_{\mathrm{L}}(x, y)$ is the local velocity in the undisturbed laminar boundary layer (indicated in Figure 4b). The velocity perturbation $\tilde{u}(x, y, t')$ quantifies the momentum excess or deficit produced by the ensemble-averaged turbulent spot. Similarly, the root-mean-square (r.m.s) velocity fluctuation of the turbulent spot at the corresponding time instance can be given by:

$$u'(x, y, t') = \frac{\sqrt{\frac{1}{N}\sum_{i=1}^{N}\left[u_i(x, y, t') - \langle u(x, y, t')\rangle\right]^2}}{U_{\infty}(x)}, \tag{2}$$

where N is the total number of turbulent spots measured. Note that the $u'(x, y, t')$ already contains non-dimensionalisation by the local freestream

velocity U_∞. Therefore, it is a measure of the turbulence intensity caused by the passage of a turbulent spot.

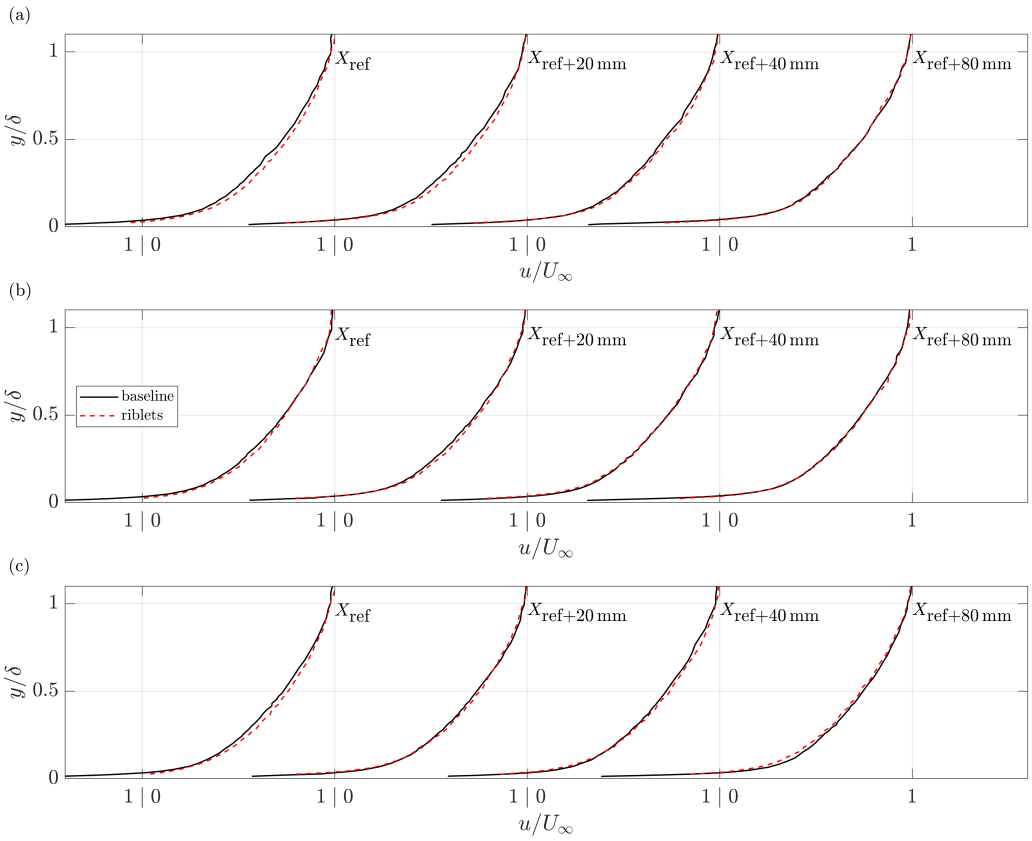

Figure 5: Turbulent boundary layer mean velocity profiles at U_∞ = (a) 10 $\mathrm{m\,s^{-1}}$, (b) 12 $\mathrm{m\,s^{-1}}$ and (c) 15 $\mathrm{m\,s^{-1}}$.

3. Results

3.1. "Stationary" turbulent boundary layer

3.1.1. Mean and turbulent velocity profiles

The velocity profiles over the test plate surfaces were measured based on the methodologies described in Section 2. As a reminder, the reference streamwise distances, X_{ref} is x = 625 mm. The first measurement point for the boundary layer profile is at X_{ref}, followed by $X_{\mathrm{ref}} + \Delta x$, where

$\Delta x = 20, 40$ and 80 mm, i.e. $x = 645$, 665 and 705 mm, respectively. All these streamwise locations are located within the riblets surface.

Figure 5 presents a summary of the streamwise development of boundary layer velocity profiles on the flat plate surface for both the baseline and riblets cases at $U_\infty = 10$, 12 and 15 $\mathrm{m\,s^{-1}}$. The wall-normal distance y is non-dimensionalised by the local boundary layer thickness, δ, while the measured velocity is non-dimensionalised by the local U_∞. This approach allows a meaningful comparison of the baseline and riblets boundary layer profiles and provides an indication of the relative development of the boundary layers. A comprehensive boundary layer parameters for each of the measurement location, including the skin friction coefficients, are provided in Table 2.

From the first glance, the boundary layer profiles for the baseline and riblets appear to be not significantly different from each other. In the near wall region of the mean velocity profiles, both display a large velocity gradient ($\partial u/\partial y$) at $y/\delta < 0.1$, which is an indication of the dominant effect of the viscous sublayer pertaining to a turbulent boundary layer where the velocity is predominantly affected by the turbulent fluid viscosity. However, a closer examination of the boundary layer profiles, especially those at X_{ref}, does reveal that the mean velocity level at the same y/δ is generally higher for the riblets plate than the baseline counterpart for a large part of y/δ. This provides a hint that the skin friction coefficient produced by the riblets plate could indeed be different. A detailed comparison of the skin friction coefficients between the baseline plate and riblets plate will be conducted later.

Figure 6 shows the turbulence intensity $u_{\mathrm{rms}}/U_\infty$ boundary layer profiles for both the baseline and riblets cases. Similarly, they are plotted against the non-dimensionalised height to compare the changes in turbulence intensity relative to the location inside the boundary layer. Unlike the mean velocity profiles, the turbulence intensity profiles demonstrate significant differences between the baseline and riblets plates across the streamwise distances.

In Figure 6a, where $U_\infty = 10$ $\mathrm{m\,s^{-1}}$, the turbulence intensity profiles develop as would be expected for a turbulent boundary layer for the baseline case. The turbulence intensity reaches a peak of $u_{\mathrm{rms}}/U_\infty \approx 11\%$ in the near wall region and decays to about 0.5% in the freestream. The location of the maximum $u_{\mathrm{rms}}/U_\infty$ is generally located at $y/\delta \approx 0.05$, which is also likely to be the location where the maximum turbulence production occurs. Below this height, the turbulence level is dissipated by the viscosity effect. Another trend is that, as U_∞ increases, the maximum level of $u_{\mathrm{rms}}/U_\infty$ also

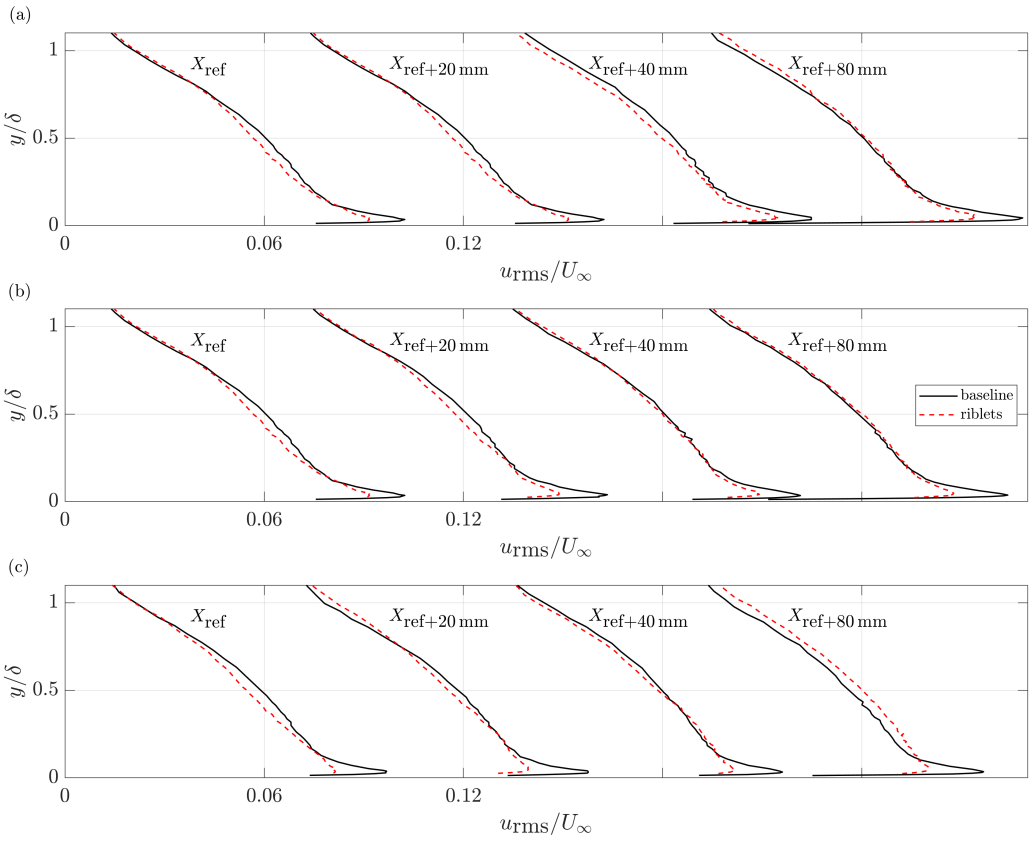

Figure 6: Turbulent boundary layer turbulent velocity profiles at U_∞ = (a) 10 m s^{-1}, (b) 12 m s^{-1} and (c) 15 m s^{-1}.

decreases (Figure 6b and 6c).

Interestingly, when the baseline turbulent boundary layer profiles are compared against the riblets case, the riblets consistently exhibit a clear reduction in the turbulence intensity level at the near wall region. For example, when $U_\infty = 10$ m s^{-1} at X_{ref}, the riblets produce a reduction in the near wall $u_{\mathrm{rms}}/U_\infty$ level by approximately 6.8% compared to the baseline case. At $X_{\mathrm{ref}} + 80$ mm, the level of reduction in $u_{\mathrm{rms}}/U_\infty$ increases to 12.4%. As the freestream velocity increases (Figure 6b and 6c), the near wall turbulence reduction by the riblets becomes even more significant. The results provide a clear indication that the current riblets surface can indeed manipulate and inhibit the turbulence production in a boundary layer under the prescribed flow conditions.

In the outer layer region of the turbulent boundary layer, the level of $u_{\mathrm{rms}}/U_\infty$ produced by the riblets is also considerably less than that produced by the baseline, especially at $x = X_{\mathrm{ref}}$ and $X_{\mathrm{ref}} + 20$ mm. This indicates that the turbulent energy transport across the entire boundary layer has been affected by the riblets. At further downstream locations of $x = X_{\mathrm{ref}} + 40$ mm and $X_{\mathrm{ref}} + 80$ mm, whilst still exhibiting lower $u_{\mathrm{rms}}/U_\infty$ level at the near wall, the turbulence level in the outer layer becomes similar (sometimes exceeds) against the baseline counterpart. A similar result was noted by Choi [18] and Yanjnik and Acharya [34], who described this increase as a natural redistribution of the turbulent kinetic energy between the inner layer and outer layer after a certain riblets length has passed.

The turbulent velocity profiles produced by the riblets can be summarised as follows: First, the near wall turbulence is very sensitive to the riblets where the reduction in the turbulence intensity level can be consistently achieved. In addition, within the coverage of the riblets the level of turbulence reduction increases at more downstream locations. Second, the sub-scale nature of the riblets is capable of extending its turbulence reduction influence to the outer layer, especially at the lower x region, i.e. the starting part of the riblets plate. This indicates that when the turbulent boundary layer is relatively small in length scale compared to the riblets height h, the disruption to the turbulence production at the near wall region can be effectively transferred to the outer layer. However, when the turbulent boundary layer grows further downstream, the effect of the riblets is mostly confined to the near wall region.

Table 2 summarises the turbulent boundary layer parameters produced by the baseline and riblets, respectively. Note that, in the table, δ^* and θ refer to the boundary layer displacement thickness and momentum thickness, respectively. A general trend discernible from the table is that the boundary layer thicknesses δ, δ^* and θ increase with x, but they will decrease with U_∞. The table also records the shape factors, H, which is defined as the ratio between the δ^* and θ. The typical shape factor of a turbulent boundary layer is $H = 1.3 \sim 1.4$ for a zero pressure gradient flow. From the table, the shape factors measured in the current study fall within an acceptable range pertaining to a fully developed turbulent boundary layer on a flat plate.

The skin friction coefficients, c_f for both the baseline and riblets are also tabulated in Table 2. The riblets consistently demonstrate a production of lower c_f than the baseline counterpart across the entire streamwise locations and freestream velocities investigated in the current study. The observation

Δx (mm)	δ (mm)	δ^* (mm)	θ (mm)	H	c_f	Δc_f (%)
$U_\infty = 10$ m s^{-1}						
0	11.352 {11.195}	1.849 {1.565}	1.362 {1.195}	1.358 {1.310}	0.00455 {0.00440}	3.297
20	12.097 {12.366}	1.932 {1.744}	1.412 {1.323}	1.368 {1.319}	0.00450 {0.00435}	3.333
40	12.633 {12.104}	1.907 {1.818}	1.391 {1.362}	1.371 {1.335}	0.00447 {0.00430}	3.803
80	13.125 {12.506}	1.984 {1.806}	1.424 {1.357}	1.394 {1.331}	0.00439 {0.00425}	3.189
$U_\infty = 12$ m s^{-1}						
0	10.857 {10.765}	1.776 {1.568}	1.314 {1.214}	1.351 {1.214}	0.00434 {0.00425}	2.074
20	11.794 {11.090}	1.839 {1.607}	1.353 {1.217}	1.359 {1.320}	0.00432 {0.00420}	2.778
40	11.950 {11.835}	1.855 {1.792}	1.366 {1.353}	1.357 {1.325}	0.00430 {0.00415}	3.488
80	12.205 {11.950}	1.941 {1.769}	1.415 {1.335}	1.371 {1.325}	0.00425 {0.00408}	4.000
$U_\infty = 15$ m s^{-1}						
0	10.503 {10.289}	1.688 {1.403}	1.260 {1.079}	1.340 {1.300}	0.00417 {0.00408}	2.158
20	10.985 {10.702}	1.730 {1.498}	1.278 {1.129}	1.353 {1.328}	0.00413 {0.00405}	1.937
40	10.846 {10.870}	1.745 {1.623}	1.299 {1.221}	1.343 {1.329}	0.00409 {0.00400}	2.200
80	11.340 {10.950}	1.767 {1.675}	1.313 {1.264}	1.346 {1.325}	0.00405 -	-

Table 2: Summary of the turbulent boundary layer parameters produced by the baseline and riblets (in braces), respectively. Δx is the distance downstream of X_{ref}.

of lower c_f produced by the riblets also correlates well with the turbulent velocity profiles, which show a reduction in the turbulence intensity level at the near wall region. From the measured data, the average skin friction reductions by the riblets Δc_f (positive value denotes reduction, and vice versa) are 3.4% at $U_\infty = 10$ m s^{-1}, 3.1% at $U_\infty = 12$ m s^{-1}, and 2.5% at $U_\infty = 15$ m s^{-1}. Hence, the effectiveness of the drag reduction capabilities of the riblets will degrade slightly as U_∞ increases. As shown in the table, a higher U_∞ would entail lower boundary layer thicknesses in δ, δ^* and θ. In other words, riblets with a fixed h at higher U_∞ will gradually be seen as a "surface roughness" instead of a sub-scale device that can restrict the wall vortices of the coherent structures. Despite only covering a relatively small U_∞ range in the current study, the inter-dependency between the boundary layer thickness and the riblets height in their skin friction production follows a clear trend.

As a summary, this sub-section focuses on the time-domain analysis of the turbulent boundary layer. The turbulence and drag reduction capabilities of the riblets designed and manufactured in-house have been positively demonstrated.

3.1.2. Wall pressure fluctuations

Figure 7 presents the wall pressure spectra at $x = X_{\text{ref}}$, X_{ref} +20 mm, and X_{ref} + 40 mm for $U_\infty = 10$, 12 and 15 m s^{-1}. The wall pressure spectra are split low/medium frequency zone at $0.2 \leq f \leq 2$ kHz, and high frequency zone at $2 \leq f \leq 6$ kHz. Three indicative lines pertaining to the frequency decay of $f^{-1/2}$, $f^{-5/3}$ and f^{-5} are included. Essentially, the wall pressure spectra show the relative energies of turbulent eddies of different scales in the boundary layer. The wall pressure spectra at lower frequency dominates the flow, which is indicative of larger size turbulent eddies. Therefore, the high frequency range is indicative of the smaller size turbulent eddies in the flow. To help with the discussion later, a generalisation is made here whereby the frequency region that contains a wall pressure spectra level decaying at $f^{-1/2}$ will be referred to as the "low frequency". Likewise, the wall pressure spectra that decay at $f^{-5/3}$ will occur at the "mid frequency". Finally, the "high" frequency turbulence decay refers to the rate of f^{-5}. Such division of frequency decays for the wall pressure spectra is also observed by Gravante *et al.* [35] for a 2D turbulent boundary layer, which has a similar flow condition to the current case. As the flow progresses downstream and the boundary layer thickness grows, the mid frequency range slowly nudges towards the

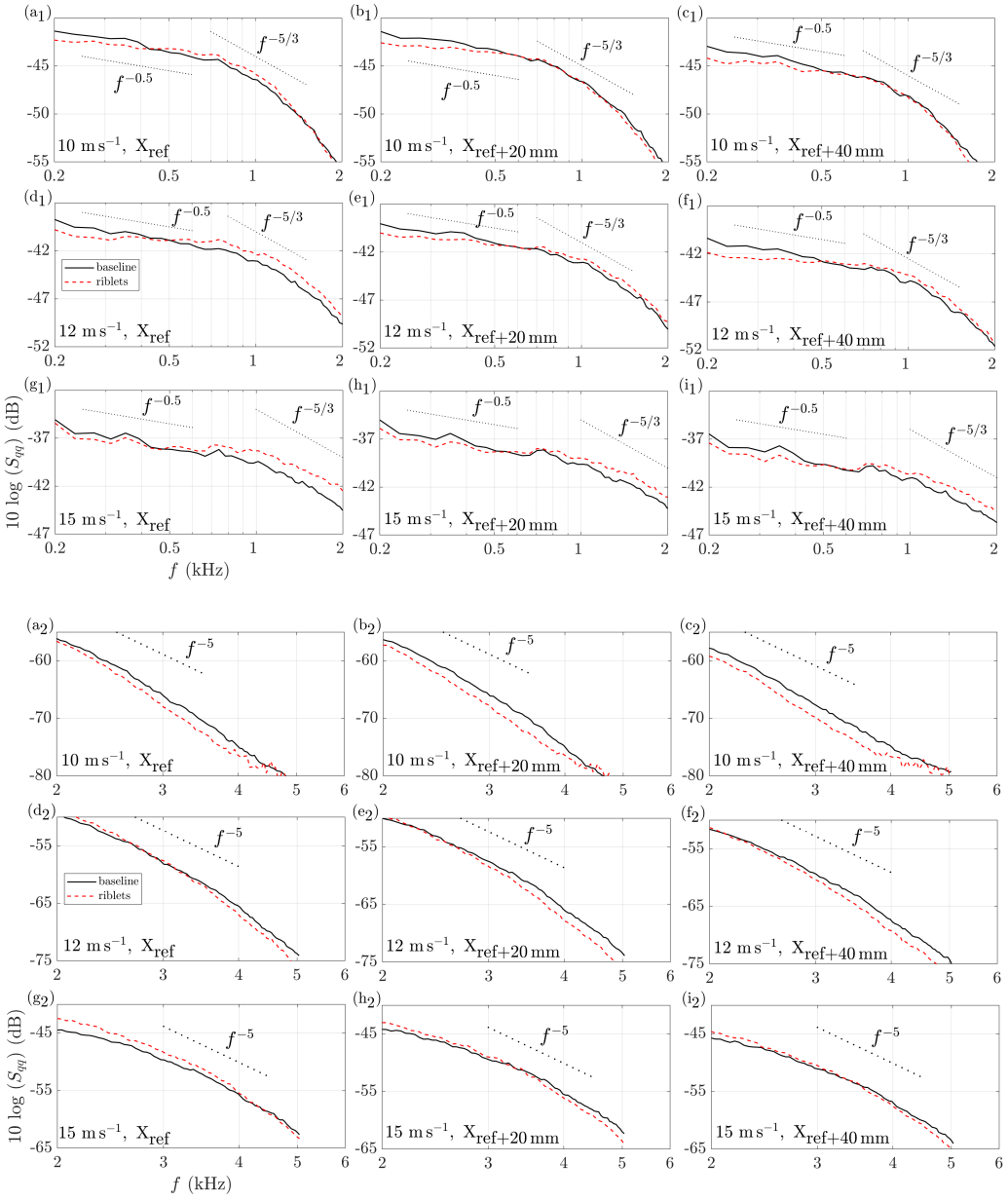

Figure 7: Comparisons of the wall pressure power spectra densities produced by the baseline and riblets surfaces. Sub-figures ($a_1 - i_1$): $0.2 \leq f \leq 2$ kHz, and ($a_2 - i_2$): $2 \leq f \leq 6$ kHz. (a_1, a_2), (b_1, b_2), (c_1, c_2): $U_\infty = 10$ m s^{-1} for (a_1, a_2) $x = X_{\text{ref}}$, (b_1, b_2) $x = X_{\text{ref}} + 20$ mm, (c_1, c_2) $x = X_{\text{ref}} + 40$ mm; (d_1, d_2), (e_1, e_2), (f_1, f_2): $U_\infty = 12$ m s^{-1} for (d_1, d_2) $x = X_{\text{ref}}$, (e_1, e_2) $x = X_{\text{ref}} + 20$ mm, (f_1, f_2) $x = X_{\text{ref}} + 40$ mm; (g_1, g_2), (h_1, h_2), (i_1, i_2): $U_\infty = 15$ m s^{-1} for (g_1, g_2) $x = X_{\text{ref}}$, (h_1, h_2) $x = X_{\text{ref}} + 20$ mm, (i_1, i_2) $x = X_{\text{ref}} + 40$ mm.

lower frequency end. This may indicate that the thickened boundary layer is a consequence of the physical enlargement of the dominant turbulent eddies.

From the first glance, the wall pressure spectra produced by both the baseline and riblets can already tell some notable differences. For both the low and high frequency ranges, the riblets produce lower wall pressure spectra level than those by the baseline counterpart. When examining the decay rates of the wall pressure spectra, the riblets have a lower energy signature at the low frequency region although the decay rate of $f^{-1/2}$ does not seem to change much. However, the turbulent energy at high frequency will dissipate faster at a decay rate slightly higher than f^{-5}. This raises a prospect that, for the case of acoustic scattering at the trailing edge whose wall pressure spectra and the scattered acoustic spectra are highly correlated, a lower level of wall pressure spectra observed in the riblets surface has a potential to cause a lower noise emission at the low and high frequency regions if the riblets are placed near an aerofoil trailing edge. The results also suggest that the riblets can manipulate more effectively for the large and small-scale turbulent eddies. However, it is important to note that the wall pressure spectra are not the only turbulent source for the far field radiation. Essentially, the lateral turbulence length scale, as a function of the frequency, is another important turbulent source for trailing edge noise. Further discussion about this will be provided later.

For some, it may be counter-intuitive that a sub-scale flow control device such as the riblets can manipulate a large-scale turbulent structure as manifested in the lower wall pressure spectral level at the low frequency. This phenomenon can be explained from a physical point of view. The low speed streaks in the near wall region of the turbulent boundary layer convecting over a riblets surface are forced into alignment and their meandering tendencies are reduced significantly. Such manipulation of the turbulent structures by the riblets is manifested in the reductions of wall pressure fluctuations at low and high frequencies, corresponding to large and small-scale turbulent eddies, respectively. Choi [18] observes that the momentum exchange between the inner and outer layers is adjusting in response to the reduced viscous layer thickness by the riblets. This process may provide modification of the turbulence structures whose turbulence energy becomes more confined to the intermediate layer corresponding to the mid frequency range for the wall pressure spectra. This is indeed reflected in the wall pressure spectra at the mid frequency range with a decay rate $\sim f^{-5/3}$, where the riblets actually produce a slight increase in the wall pressure spectra level when compared

against the baseline counterpart in some cases.

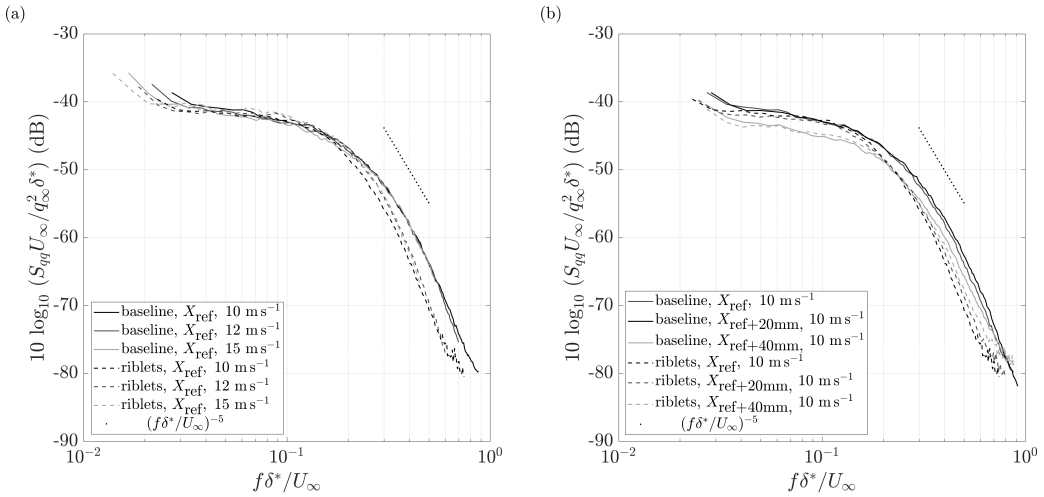

Figure 8: Comparisons of the normalised wall pressure spectra for both the baseline and riblets at (a) $x = X_{\mathrm{ref}}$, and $U_\infty = 10$, 12 ad 15 m s^{-1}, and (b) $U_\infty = 10$ m s^{-1}, and $x = X_{\mathrm{ref}}$, $X_{\mathrm{ref}} + 40$ mm, and $X_{\mathrm{ref}} + 80$ mm.

The next step is to examine the wall pressure spectra in a non-dimensional form for both the baseline and riblets cases. The scaling parameters are chosen as the outer variables, whereby the spectra is normalised using q_∞ ($= \frac{1}{2}\rho U_\infty^2$) as the pressure scale, and $\frac{\delta^*}{U_\infty}$ as the time scale. Accordingly, the frequency is non-dimensionalised by the inverse of the time scale. Figure 8a represents the non-dimensionalised wall pressure spectra at $x = X_{\mathrm{ref}}$ for $U_\infty = 10$, 12 ad 15 m s^{-1}. For the baseline case, the spectra collapse well for most of the scaled-frequency range, including those at the high frequency despite using the outer-layer variables. The decay rate at the high frequency again follows $(\frac{f\delta^*}{U_\infty})^{-5}$. The riblets case itself also features a good collapse of the spectra throughout the non-dimensional frequency range across the freestream velocities, but the decay rate at the high frequency becomes slightly higher. The results illustrate that the small-scale turbulent eddies can be attenuated more effectively by the riblets when compared to the baseline.

When the comparison of the wall pressure spectra between the baseline and riblets is made in the dimensional spectral level and frequency, the implication could be quite different when the same comparison is made in non-dimensional spectral level and frequency. For example, one could com-

pare the dimensional (Figure $7g_1$ and $7g_2$) and non-dimensional (Figure 8a) spectra for the case of $x = X_{\text{ref}}$ and $U_\infty = 15$ m s^{-1}: when compared to the spectrum produced by the baseline in dimensional form, the riblets demonstrate a slightly lower spectral level at the low frequency ($f < 650$ Hz), higher spectra level at the mid frequency ($650 < f < 4000$ Hz), and then a slightly lower spectral level at the high frequency ($f > 4000$ Hz). However, when plotted in non-dimensional form, the scaled spectra between the riblets and baseline seem to "nudge" towards each other in the frequency-domain in such a way that they now collapse well at $\frac{f\delta^*}{U_\infty} < 0.2$, but a much larger level of reduction for the scaled spectral level is demonstrated by the riblets at $\frac{f\delta^*}{U_\infty} > 0.2$. This lends support to our earlier description that the riblets can affect both the inner and outer parts of a boundary layer by disrupting the momentum exchange between them. Further examination of this mechanism will be discussed in Section 3.2 when the investigation turns to the temporal development of turbulent spots on the riblets surface.

Figure 8b examines the scalability of the spectral level and frequency as a function of streamwise distance ($x = X_{\text{ref}}$, $X_{\text{ref}} + 20$ mm, $X_{\text{ref}} + 40$ mm) under a single freestream velocity of $U_\infty = 10$ m s^{-1}. This is basically a re-plot of Figure $7a_1 - c_1$ and $7a_2 - c_2$ in a non-dimensional form. In Figure 8b, the collapse of the scaled spectra at $\frac{f\delta^*}{U_\infty} < 0.2$ can be repeated. However, at $\frac{f\delta^*}{U_\infty} > 0.2$, the riblets that were originally shown to be effective in producing a lower wall pressure spectral level (scaled) at $x = X_{\text{ref}}$ become less effective at downstream location of $x = X_{\text{ref}} + 40$ mm. This illustrates that as the boundary layer on the riblets surface becomes thicker, the ability of the riblets to manipulate the turbulent structures becomes weaker, which is reflected by the wall pressure spectra slowly conforming to that of the baseline's.

3.1.3. Streamwise cross-correlations, convection velocities and streamwise coherence function

$$R_{x_i x_j}(\tau) = \frac{\overline{p'_{x_i}(x_i, t)\, p'_{x_j}(x_j, t-\tau)}}{p'_{x_i,\text{rms}}(x_i)\, p'_{x_j,\text{rms}}(x_j)}. \tag{3}$$

The streamwise cross-correlation coefficient $R_{x_i x_j}$ is defined in Equation 3, which can be used to measure the turbulence decay in the temporal domain between two wall fluctuating pressure measurement points. In the equation, p'_{x_i} and p'_{x_j} are the wall pressure fluctuations from the remote microphone

sensors i and j situated at locations x_i and x_j, respectively. Likewise, $p'_{x_i,\mathrm{rms}}$ and $p'_{x_j,\mathrm{rms}}$ are the root mean square values of the pressure fluctuations measured by the remote microphone sensors i and j respectively. τ is a time delay between the signals, and the overbar denotes time averaging.

In the present experiments, all the streamwise cross-correlation studies were conducted by taking reference to the most upstream microphone sensor at $x = X_{\mathrm{ref}}$. Therefore, Δx denotes the streamwise distance from X_{ref}. Figure 9a plots the maximum normalised cross-correlation coefficients, $R_{x_i x_j\,(\max)}$, against their corresponding time delay $\tau_{\,(\max)}$ for various $\Delta x/\delta^*_{(\mathrm{ref})}$ locations at $U_\infty = 12\ \mathrm{m\,s^{-1}}$. Note that $\delta^*_{(\mathrm{ref})}$ is the displacement thickness of the boundary layer measured at X_{ref}. The auto-correlation peak is omitted as by default it has a maximum value of $R_{x_i x_j\,(\max)} = 1$ at $\tau_{\,(\max)} = 0$.

From Figure 9a, the decay of $R_{x_i x_j\,(\max)}$ against the $\tau_{\,(\max)}$ is linear for both the baseline and riblets, but the riblets consistently produce lower level of the $R_{x_i x_j\,(\max)}$ when compared to those produced by the baseline. The difference between them is in the region of $3.2 \sim 8.3\%$. A reduced level of $R_{x_i x_j\,(\max)}$ achieved by the riblets may be interpreted as a more effective breakdown of the turbulence structures. This phenomenon is consistent for other freestream velocities at $U_\infty = 10$ and $15\ \mathrm{m\,s^{-1}}$, but the results are not shown here for brevity.

The next step is to investigate whether achieving a more rapid breakdown of the turbulence structures by the riblets can also affect the turbulence convection velocity. From a dataset of $(\Delta x, \tau)$, an average convection velocity of the dominant turbulent eddies can be determined. It should be noted that the most dominant turbulent eddies in the boundary layer would decay at a slower rate than the small-scale turbulent eddies. Figure 9b presents several linear best fit lines for the datasets of Δx against $\tau_{\,(\max)}$. The gradients of the best fit lines represent the convection velocity of the most dominant turbulence structures, which will increase proportionally with U_∞. From the figure, the comparison suggests that there is not a huge difference in the convection velocities of the dominant turbulence structures between the baseline and riblets. The measured turbulence convection velocities are between $0.8U_\infty$ and $0.88U_\infty$.

$$\gamma^2_\kappa\,(f) = \frac{\left|\Phi_{\kappa_i\kappa_j}(f)\right|^2}{\Phi_{\kappa_i\kappa_i}(f)\ \Phi_{\kappa_j\kappa_j}(f)}\ , \qquad \kappa = x \text{ or } z. \tag{4}$$

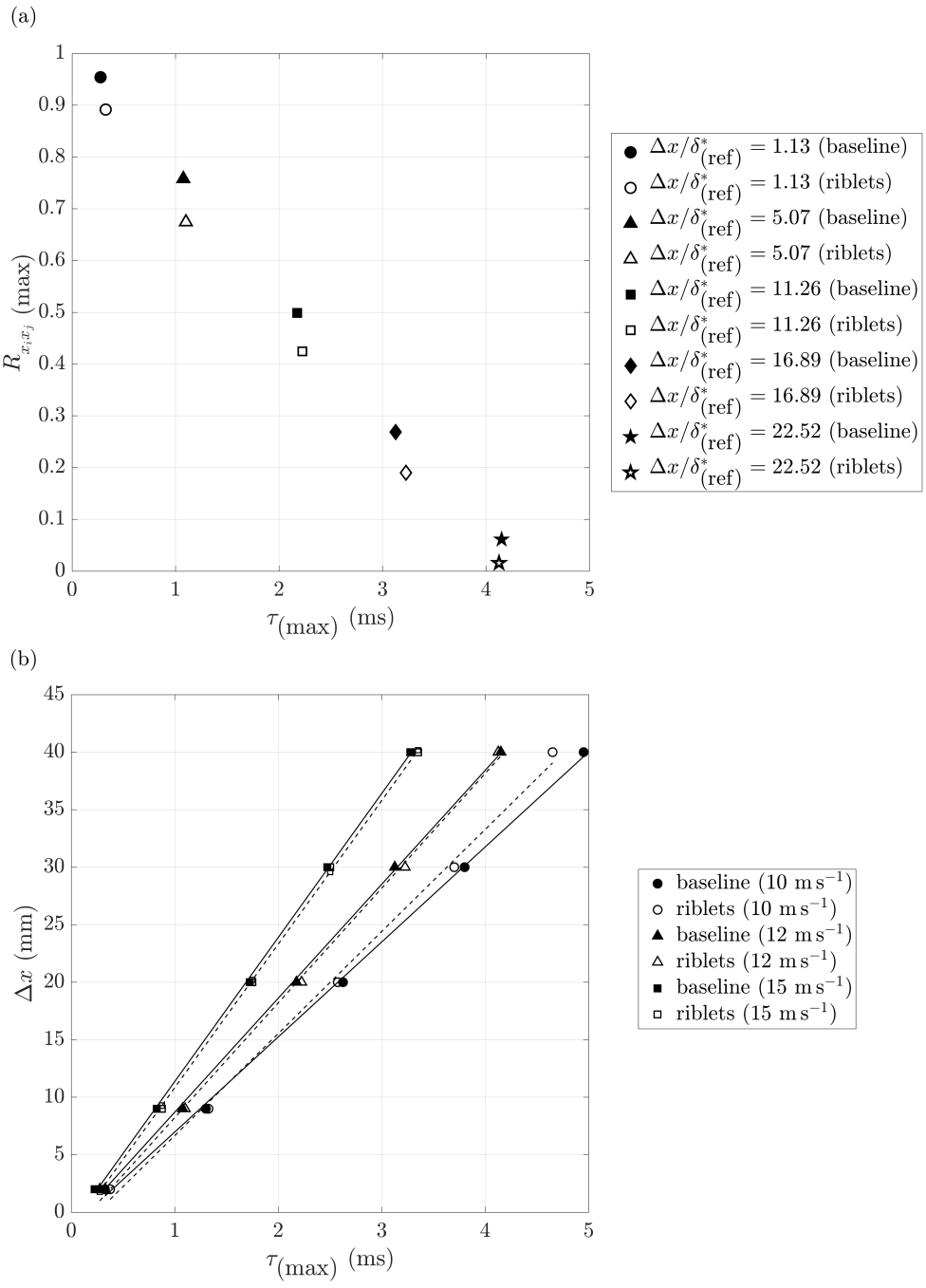

Figure 9: Comparisons between the baseline and riblets for their (a) streamwise cross-correlation coefficient maxima $R_{x_i x_j\,(\max)}$ against their corresponding time delay $\tau_{\,(\max)}$ at $U_\infty = 12$ m s^{-1}, and (b) turbulent eddies convection velocities at $U_\infty = 10, 12$ and 15 m s^{-1}.

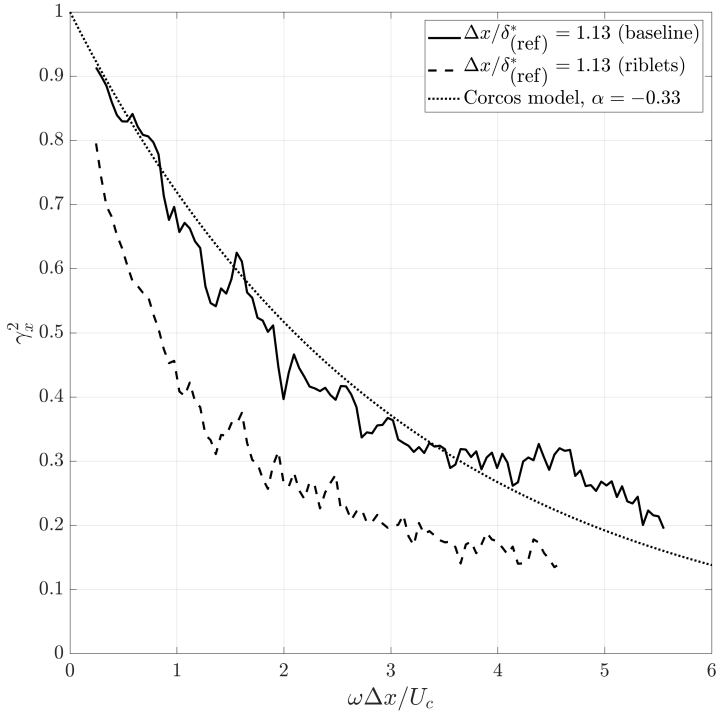

Figure 10: Comparisons between the baseline and riblets for their streamwise coherence γ_x^2 at $U_\infty = 12\ \mathrm{m\,s^{-1}}$.

The *likeness* of the wall pressure fluctuation signals between two microphone sensors in the frequency domain can be defined by the magnitude squared coherence of two microphone signals, $\gamma_\kappa^2(f)$, which is described by Equation 4. $\Phi_{\kappa_i\kappa_j}(f)$ is the cross power spectral density between two wall pressure fluctuating signals at locations κ_i and κ_j, where κ can be either x or z. The wall pressure signal at κ_i is usually designated as the reference microphone sensor located at $x = X_{\mathrm{ref}}$, which is also at the mid-span ($z = 0$) of the flat plate. Therefore, $\Phi_{\kappa_i\kappa_i}(f)$ and $\Phi_{\kappa_j\kappa_j}(f)$ are the auto power spectral density for the reference (i) and j^{th} wall pressure fluctuations, respectively.

According to Brooks and Hodgson [36], γ_x^2 (magnitude squared streamwise coherence spectra) describe the lifespan of turbulent eddies in the flow filed. Figure 10 compares the γ_x^2, as a function of $\omega\Delta x/U_c$, between the baseline and riblets at $U_\infty = 12\ \mathrm{m\,s^{-1}}$, where ω is the angular frequency, and U_c is the convection velocity of the turbulent eddies. The discussion will first focus on the γ_x^2 spectra for the baseline case. Based on the similarity

of turbulence decay, an exponential function has been proposed by Corcos [37] in the form of $\exp(-\alpha\omega\Delta x/U_c)$ to describe the streamwise coherence, where α is an empirical constant. At $\Delta x = 2$ mm, or $\Delta x/\delta^*_{(\mathrm{ref})} = 1.13$, a decay of coherence has already been registered in the convecting pressure field. The γ_x^2 curve can be fitted well by the Corcos' exponential function when $\alpha = -0.33$ and $U_c = 0.84U_\infty$. The good match also holds true for other U_∞ investigated in this study (not shown here for brevity).

Now, the analysis will focus on the comparison of the γ_x^2 between the baseline and riblets. Figure 10 clearly shows that the riblets can achieve a significant reduction of the coherence level for the wall pressure fluctuations across almost the entire range of frequency. This indicates that a significant cascade of turbulence length scales has been manipulated even at the early stage of the riblets. Although not shown here, the level of difference in the γ_x^2 between the baseline and riblets, as a function of frequency, increases as U_∞ increases. This could be due to the fact that the riblets is more effective when the ratio between the riblets height and boundary layer thickness increases. However, it should also be noted that such ratio should not be too large as the riblets could switch its role from a drag-reducing device to a turbulence-enhancing surface roughness.

As a summary, the wall turbulence can react rapidly to the riblets in three ways: hastening the decline of the streamwise coherence function, reduction of the turbulence lifespan and de-correlation of the turbulent eddies. Although the riblets can manipulate a wall turbulence structure in the longitudinal direction, as well as reduce the r.m.s. longitudinal velocity fluctuations in the boundary layer significantly (Figure 6), it does not result in a significant reduction of the wall pressure spectra level at the mid-frequency region associated with the $f^{-5/3}$ decay (Figure 7), nor the convection velocity pertaining to the most dominant turbulence structures. It is known that the wall pressure fluctuations are pre-dominantly contributed by the velocity fluctuations in the wall-normal direction, e.g. the wall-inward sweeping and ejection events during the re-generation cycle of the coherent structures. Although the riblets can change the turbulence structure in the convective field (i.e. its longitudinal structure), and reduce the overall boundary layer thicknesses (see Table 2), it may not yet be sufficient to fundamentally alter the turbulence re-generation mechanism.

3.1.4. Spanwise coherence function and coherence length scale

Another parameter that is appropriate to describe a turbulence structure and its physical size in the frequency domain is the spanwise (lateral) coherence function, γ_z^2, which is also described in Equation 4 when $\kappa = z$. As will be discussed later, the spanwise coherence function is also related to the lateral length scale of the turbulence, which is one of the key turbulent sources for the trailing edge noise radiation. How the spanwise coherence of the turbulence structures reacts to the riblets is of interest in this study.

Figure 11 shows the spanwise coherence spectra between the baseline and riblets cases at $U_\infty = 10, 12$ and $15\ \mathrm{m\,s^{-1}}$. The spanwise coherence is described by $\Delta z/\delta^*_{(\mathrm{ref})}$, which now denotes the normalised lateral distance between the reference microphone at X_{ref} and another microphone under

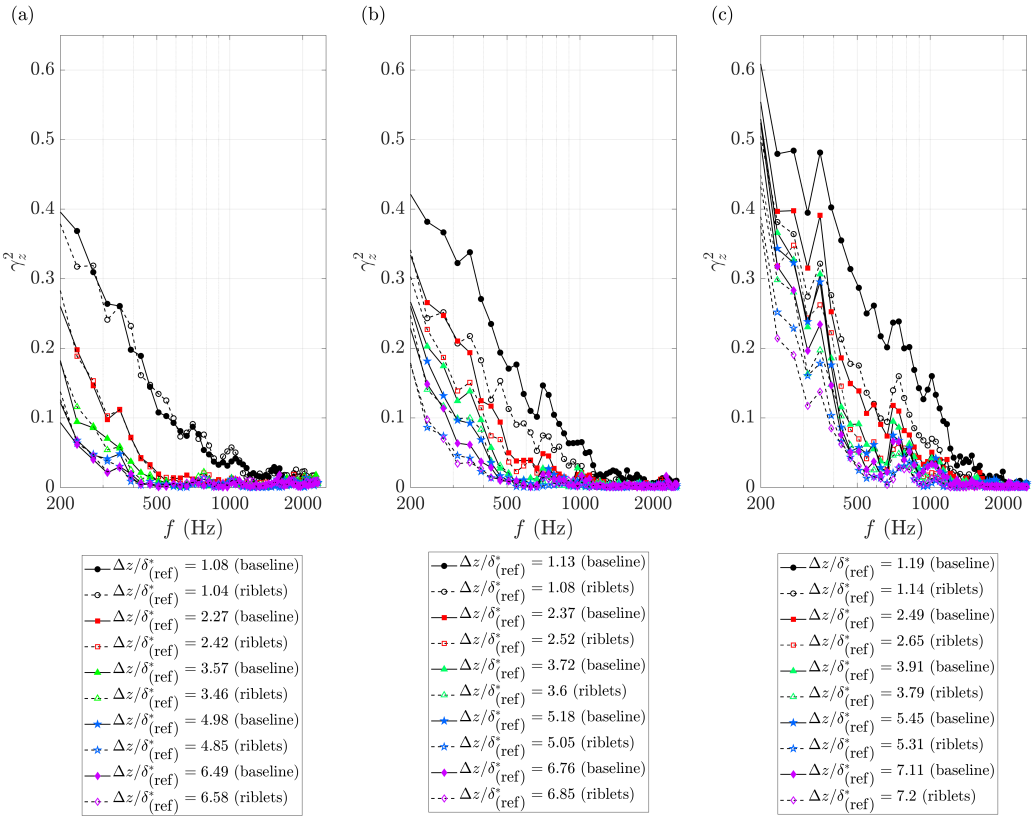

Figure 11: Comparisons between the baseline and riblets for their spanwise coherence γ_z^2 at U_∞ = (a) $10\ \mathrm{m\,s^{-1}}$, (b) $12\ \mathrm{m\,s^{-1}}$ and (c) $15\ \mathrm{m\,s^{-1}}$.

question. The overall coherence level reduces as the lateral separation distance $\Delta z/\delta^*_{(\mathrm{ref})}$ increases. This phenomenon demonstrates that, as the spanwise separation increases, the level of *likeness* of the turbulence will decrease. At $U_\infty = 10\ \mathrm{m\,s^{-1}}$, the spanwise coherence produced by the riblets between $2.42 \leq \Delta z/\delta^*_{(\mathrm{ref})} \leq 6.58$ are almost identical to those of the baseline, suggesting that the turbulence structures maintain the same degree of lateral order as the riblets case. This means that the fundamental turbulence regeneration mechanism remains unaffected, which is supported by the fact that, at this particular freestream velocity, the riblets are incapable of altering the wall fluctuating pressure spectra at the mid frequency region as shown in Figure $7\mathrm{a}_1 - \mathrm{c}_1$.

However, at $U_\infty = 12$ and $15\ \mathrm{m\,s^{-1}}$, the level of spanwise coherence achieved by the riblets becomes consistently lower than the baseline counterparts, especially when $\Delta z/\delta^*_{(\mathrm{ref})}$ is between 1.08 and 1.14 where large reduction has been achieved. This implies that the fundamental turbulence structure at higher freestream velocities, which would entail a lower growth rate of turbulent boundary layer thickness, can be more readily altered by the riblets. This is also manifested by the quantifiable changes in the wall fluctuating pressure spectra at the mid frequency shown in Figure $7\mathrm{d}_1 - \mathrm{f}_1$ and Figure $7\mathrm{g}_1 - \mathrm{i}_1$. Hence, it seems that the wall pressure spanwise coherence and power spectral density become more sensitive to the riblets when $U_\infty > 12\ \mathrm{m\,s^{-1}}$. A plausible explanation for the disparity of results between Figure 11a and Figure 11b/c could be related to the reduction of boundary layer thickness as U_∞ increases. After examination of the tabulated values in Table 2 in conjunction with the current riblets whose height is fixed at h = 0.36 mm, a condition of $h/\delta^* > 0.2$ must be fulfilled for the riblets so that they will gain the capability to affect the wall pressure spanwise coherence and power spectral density. Note that this condition applies to the wall pressure fluctuation only and may not be applicable to the velocity fluctuation levels within the turbulent boundary layer as shown in Figure 6.

$$l_z(f) = \int_0^\infty \sqrt{\gamma_z^2(z,f)}\,\mathrm{d}z. \tag{5}$$

The spanwise coherence γ_z^2 does not measure any convective components of the turbulence structures. Instead, it mostly contains information about the physical size of the turbulent eddies. As described in Equation 5, an integration of the spanwise coherence magnitude across the lateral location

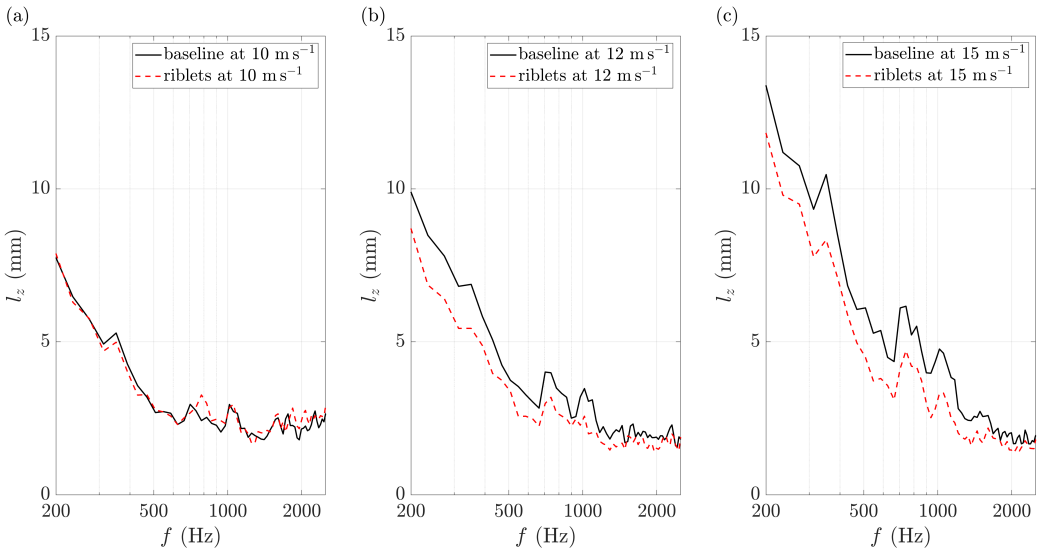

Figure 12: Comparisons between the baseline and riblets for their spanwise coherence length $l_z(f)$ at U_∞ = (a) 10 m s^{-1}, (b) 12 m s^{-1} and (c) 15 m s^{-1}.

can result in the lateral coherence length of the turbulence, l_z, as a function of frequency. In the current work, a total of seven different Δz are used for the calculation of the l_z. Although seven cases of Δz might not be the most abundant, any possible quantification error will not affect the current purpose because the aim is to compare the turbulence length scales produced by the baseline and riblets, respectively. In other words, the context is relative, not absolute.

As shown in Figure 12a, the l_z spectra for both the baseline and riblets at $U_\infty = 10$ m s^{-1} are very similar, as expected from the corresponding spanwise coherence spectra in Figure 11a. When the U_∞ increases to 12 and 15 m s^{-1} in Figure 12b and 12c, respectively, both demonstrate a lower l_z and reduced size of the turbulence structure when the riblest are introduced.

As a summary, reduction of the turbulence spanwise length scale can be realised by the riblets provided that $h/\delta^* > 0.2$. However, one should also be cautious that h/δ^* should not be too large in order to avoid the riblets becoming a surface roughness.

3.1.5. Implications to the self-noise radiation

The relationship between the far field pressure (i.e. noise) and the near field wall pressure fluctuation near the trailing edge of an aerofoil is made

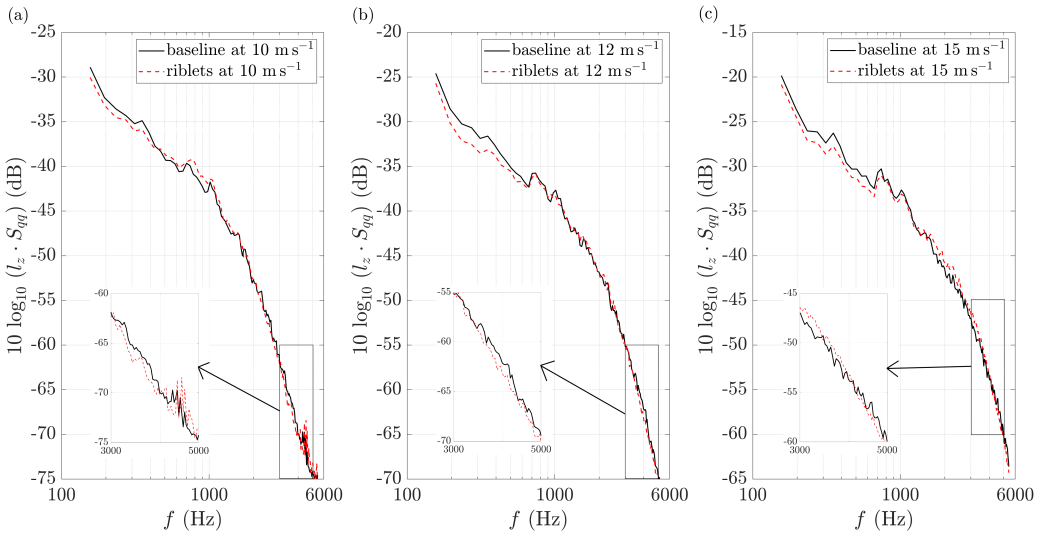

Figure 13: Partial turbulent noise sources of 10 $\log_{10}(l_z \cdot S_{qq})$ based on Amiet's trailing edge noise model at U_∞ = (a) 10 m s^{-1}, (b) 12 m s^{-1} and (c) 15 m s^{-1}. The spectra are measured at the reference location X_{ref}.

explicit in the classical work of Amiet [38], who derived a direct relationship between the power spectral density of the far field trailing edge noise (S_{pp}) of an aerofoil for an observer in the centre-line plane of an aerofoil with span $2d$, chord, $2b$, to the wall pressure spectra (S_{qq}) by:

$$S_{pp}(x, 0, y, \omega) = \left(\frac{\omega b y}{2\pi c_o \sigma^2}\right)^2 d|\mathfrak{L}|^2 \, l_z(\omega) S_{qq}(0, \omega), \tag{6}$$

where ω is the angular frequency, σ^2 is a Mach number corrected geometrical function, and $|\mathfrak{L}|$ is the norm of the acoustical transfer function. From Equation 6, the product of the lateral coherence length (l_z) and wall pressure spectra (S_{qq}) represents the main combined sources of the radiated spectrum (S_{pp}). Although no aeroacoustics measurement on aerofoil is performed in this study, it is still possible to evaluate the effect of riblets on the trailing edge noise radiation by examining the 10 $\log_{10}(l_z \cdot S_{qq})$, as a function of frequency.

Figure 13 presents the 10 $\log_{10}(l_z \cdot S_{qq})$ at X_{ref} between the baseline and riblets at U_∞ = 10, 12 and 15 m s^{-1}. For all the cases examined here, reductions of the 10 $\log_{10}(l_z \cdot S_{qq})$ by the riblets are evident at the low frequency range ($150 < f < 600$ Hz). This outcome is expected because both the

turbulent sources S_{qq} and l_z at the corresponding frequency range are lower than those produced by the baseline. The result suggests that reduction of the trailing edge noise by riblets at low frequency is possible. For the mid frequency range, however, the riblets will either produce a similar, or slightly higher levels of $10\log_{10}(l_z \cdot S_{qq})$ compared to the baseline due to the *counter-balancing* effect between the S_{qq} and l_z: whilst the l_z can be reduced by the riblets, the corresponding S_{qq} actually undergoes an increase in level. At the high frequency range, the positive effect of the riblets in reducing the turbulent sources is again manifested by the production of lower level of $10\log_{10}(l_z \cdot S_{qq})$ as emphasised by the magnified views in the inserted plots.

It is worth mentioning that the capability of the riblets to reduce the high frequency noise weakens as the freestream velocity increases (e.g. the case of $U_\infty = 15\,\mathrm{m\,s^{-1}}$). This is due to the thinning of the turbulent boundary layer thickness, which will then increase the level of wall pressure fluctuations. The readers can compare Figure $7a_2$, $7d_2$ and $7g_2$. In other words, the thinned turbulent boundary layer reacts to the riblets as a surface roughness.

3.2. "Dynamic" turbulent boundary layer - analysis based on turbulent spots convecting over a riblets surface

Sections 3.1.1 and 3.1.3 provide sufficient evidences to prove that riblets can reduce both the longitudinal turbulence intensity level and streamwise coherence function in a fully-developed turbulent boundary layer. To understand the fundamental mechanisms that cause the above hydrodynamic responses, this section will study the spatio-temporal evolution of turbulent spots convecting over a riblets surface in an otherwise laminar boundary layer. Table 3 summarises the parameters pertaining to the laminar boundary layer for both the baseline and riblets cases. Note that the freestream velocity is set at $U_\infty = 7\ \mathrm{m\,s^{-1}}$. The typical shape factor of a Blasius laminar boundary layer is $H = 2.59$. From Table 3, the shape factor is between $2.113 \leq H \leq 2.170$. Such a small deviation from the Blasius boundary layer could be due to the presence of small level of favourable pressure gradient along the flat plate surface.

3.2.1. Spatio-temporal development of turbulent spots on riblets surface

Figure 14 represents the velocity perturbation contours of a turbulent spot at the plane of symmetry at $X_{\mathrm{ref}} + 40$ mm over the baseline surface. The spatio and temporal domains that feature $\tilde{u} \approx 0$ are representing the unperturbed laminar field. In order to depict the shape of the turbulent spot,

Δx (mm)	δ (mm)	δ^* (mm)	θ (mm)	H
0	5.584 {5.529}	1.610 {1.504}	0.762 {0.730}	2.113 {2.059}
40	5.638 {5.442}	1.658 {1.503}	0.764 {0.737}	2.170 {2.040}
80	5.851 {5.241}	1.689 {1.417}	0.784 {0.723}	2.154 {1.960}
100	5.702 {6.250}	1.641 {1.955}	0.770 {0.827}	2.132 {2.365}

Table 3: Summary of the laminar boundary layer parameters produced by the baseline and riblets (in braces), respectively. Δx is the longitudinal distance downstream of X_{ref}.

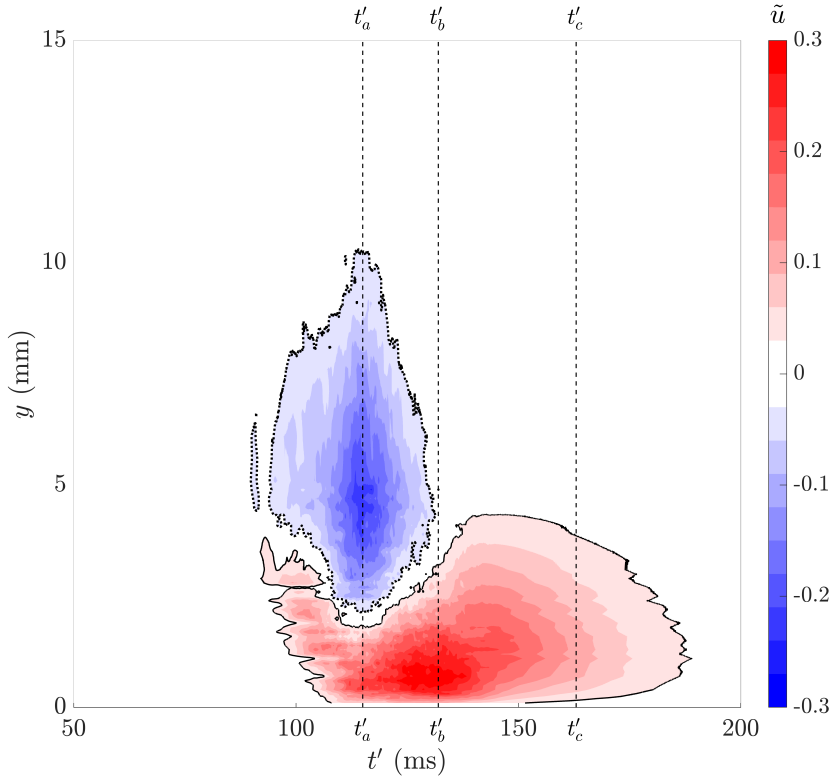

Figure 14: Contour of the velocity perturbation $\tilde{u}$ of a turbulent spot at the plane of symmetry developed on the baseline surface at $x = X_{\text{ref}} + 40$ mm. Note that the solid line represents threshold of $\tilde{u} = +0.03$, and the dotted line represents threshold of $\tilde{u} = -0.03$.

thresholds of $\tilde{u} = \pm 0.03$ are applied in the contour. Note that $\tilde{u} = +0.03$ is represented by a solid line, whereas a dotted line is used for the identification of $\tilde{u} = -0.03$. The ensemble-averaged turbulent spot displays four distinctive regions: (1) the near wall region that is dominated by the high level of *positive perturbations*, i.e. $\tilde{u} > 0$, and (2) the outer region where the velocity perturbations are predominantly *negative*. This reflects very well of a typical turbulent boundary layer velocity profile that exhibits near wall velocity excess and outer layer velocity deficit. At some intermediate heights from the surface, the turbulent spot will encounter both positive and negative perturbations along its length. These intermediate heights also coincide with the (3) *leading edge overhang* of the turbulent spot. Here, the leading edge overhang is formed by the upstream 'ejections' of turbulent fluid with sufficient energy from the near wall region to beyond the edge of the laminar boundary layer. Although the ejected turbulent fluid propagates faster than the main body of the turbulent spot, it has no self-regeneration mechanism outside the boundary layer so it will gradually decay and join the nose of the turbulent spot to form an overhang. Another important feature pertaining to a turbulent spot that is discernible from the velocity perturbation contours is the presence of a (4) *becalmed region* that corresponds to a slow recovery of velocity at the aft of each turbulent spot. The becalmed region is formed by the downstream 'sweeping' of high momentum fluid from the freestream towards the near wall of the turbulent spot's trailing edge. From the perspective of the velocity perturbation, it is difficult to distinguish the interface separating the becalmed region and the trailing edge of the turbulent spot. However, the becalmed region has a fuller velocity profile that is even more stable than the local laminar boundary layer profile. The overall shape of the velocity perturbation contour and main features agree well with the literature [20, 39, 40].

The next step is to compare the spatio-temporal development of the turbulent spots when they convect over the baseline and riblets surface, respectively. Figure 15 compares the variation of the velocity perturbation $\tilde{u}$ between the baseline and riblets cases at three *spatial* distances $x = X_{\text{ref}}, X_{\text{ref}} + 40$ mm and $X_{\text{ref}} + 80$ mm, across three *time* instances at $t' = t'_a$, t'_b and t'_c. As illustrated in Figure 14, t'_a is associated with the time instance pertaining to the maximum height of the turbulent spot, as well as where the largest level of negative perturbation occurs at the outer layer. t'_b corresponds to the time instance when the largest level of positive perturbation is recorded at the near wall region. Finally, t'_c corresponds to the becalmed

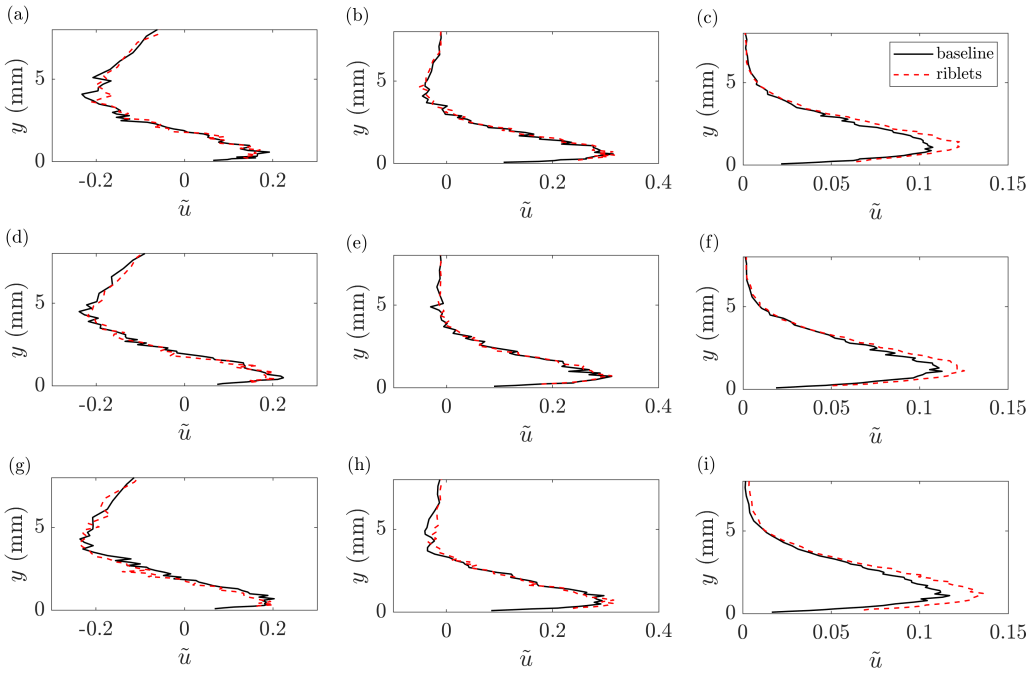

Figure 15: Presentation of $\tilde{u}$ as a function of y at (a), (b), (c): $x = X_{\text{ref}}$, for (a) $t' = t'_a$, (b) $t' = t'_b$, (c) $t' = t'_c$; (d), (e), (f): $x = X_{\text{ref}} + 40$ mm, for (d) $t' = t'_a$, (e) $t' = t'_b$, (f) $t' = t'_c$; (g), (h), (i): $x = X_{\text{ref}} + 80$ mm, for (g) $t' = t'_a$, (h) $t' = t'_b$, (i) $t' = t'_c$.

region of the turbulent spot. It is important to note that t'_a, t'_b and t'_c are the characteristic temporal quantities for the depiction of different salient features of a turbulent spot. Therefore, their values in t' will vary at different x.

Across all the spatial distances examined, the velocity perturbation profiles at t'_a and t'_b, both of which are in the main body of the turbulent spot, exhibit similarity between the baseline and riblets cases. However, at t'_c, the riblets case clearly demonstrates a larger peak of the positive velocity perturbation level than the baseline case. This enhanced peak is also elevated further away from the riblets surface. This suggests that when a turbulent spot is convecting over a riblets surface, it can induce a stronger sweeping event and larger momentum flow to enhance the local stability of the boundary layer near the spot's trailing edge. This important feature will be discussed again after the r.m.s. velocity fluctuation u' of the turbulent spot is discussed next.

Figure 16 shows the contour of the r.m.s velocity fluctuation u' for the same turbulent spot of the baseline case demonstrated earlier in Figure 14. The turbulent spot delineated by the turbulence intensity, though well defined, is quite different from that delineated by the velocity perturbation. Nevertheless, the salient features such as the leading edge, including its overhang, the maximum height and the trailing edge are all distinguishable from the r.m.s velocity fluctuation contours. However, as expected, the becalmed region is no longer discernible because by definition the turbulence intensity level at the becalmed region is very low.

The r.m.s velocity fluctuation shows that the leading edge at the near wall region, and underneath the overhang, is characterised by very high turbulence intensities between $10 \sim 14\%$. This region is herein called the *primary turbulence intensity*, which can also be found at other streamwise locations. The presence of a primary turbulence intensity within a turbulent spot is consistent with Gad-el-Hak *et al.* [41] and Glezer *et al.* [32] who observe that a strong destabilising regime is located at the leading edge interface under the overhang. This concentrated region is where the turbulence is produced, consistent with the earlier explanation of the near wall ejection of turbulent fluid that will eventually lead to the formation of a leading edge overhang. The presence of the primary turbulence intensity is needed for the destabilisation of the surrounding laminar boundary layer. High and concentrated *secondary turbulence intensity* ($8 \sim 10\%$) is also found to encompass regions that would otherwise coincide with the prominent negative perturba-

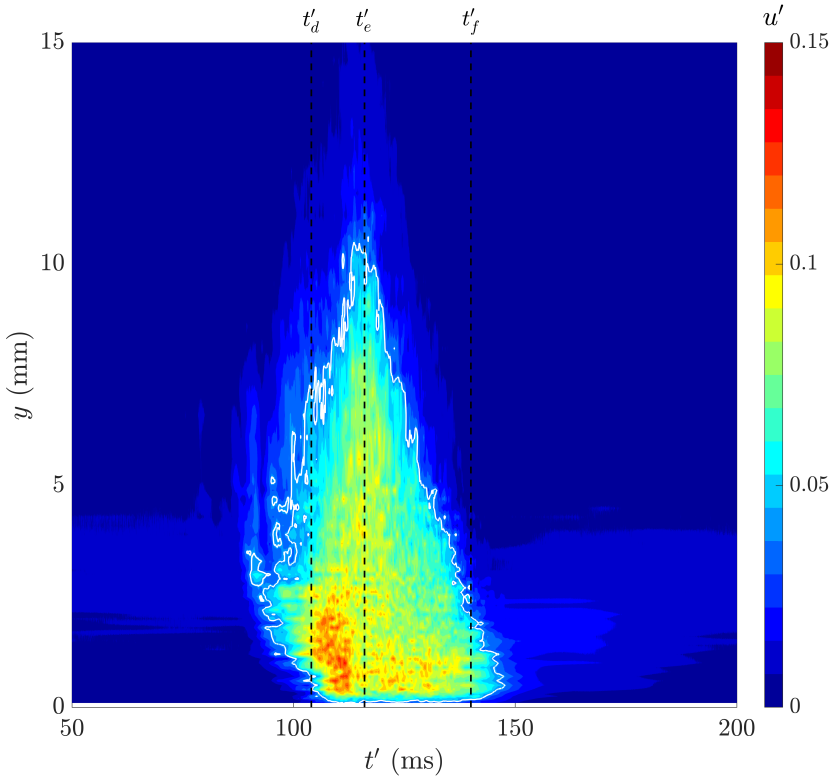

Figure 16: Contour of the r.m.s velocity fluctuation u' of a turbulent spot at the plane of symmetry developed on the baseline surface at $x = X_{\text{ref}} + 40$ mm. Note that the solid white line represents threshold of $u' = 0.04$.

tion region (at the outer layer, corresponding to t'_a) and positive perturbation region (near wall, corresponding to t'_b).

The spatio-temporal development of the turbulent spots in the context of r.m.s velocity fluctuation is examined in Figure 17 for both the baseline and riblets cases. While the spatial range in x remains the same, the characteristic t' is re-defined in accordance to the salient characteristics of u'. As illustrated in Figure 16, t'_d is associated with the time instance pertaining to the leading edge overhang of the turbulent spot. t'_e corresponds to the time instance when the maximum height of the turbulent spot occurs. Finally, t'_f corresponds to the trailing edge of the turbulent spot. Similarly, t'_d, t'_e and t'_f for each spatial distance x would entail different value of t'.

It becomes apparent that the leading edge (t'_d) and main body (t'_e) of the turbulent spots, which coincide with the aforementioned *primary turbulence*

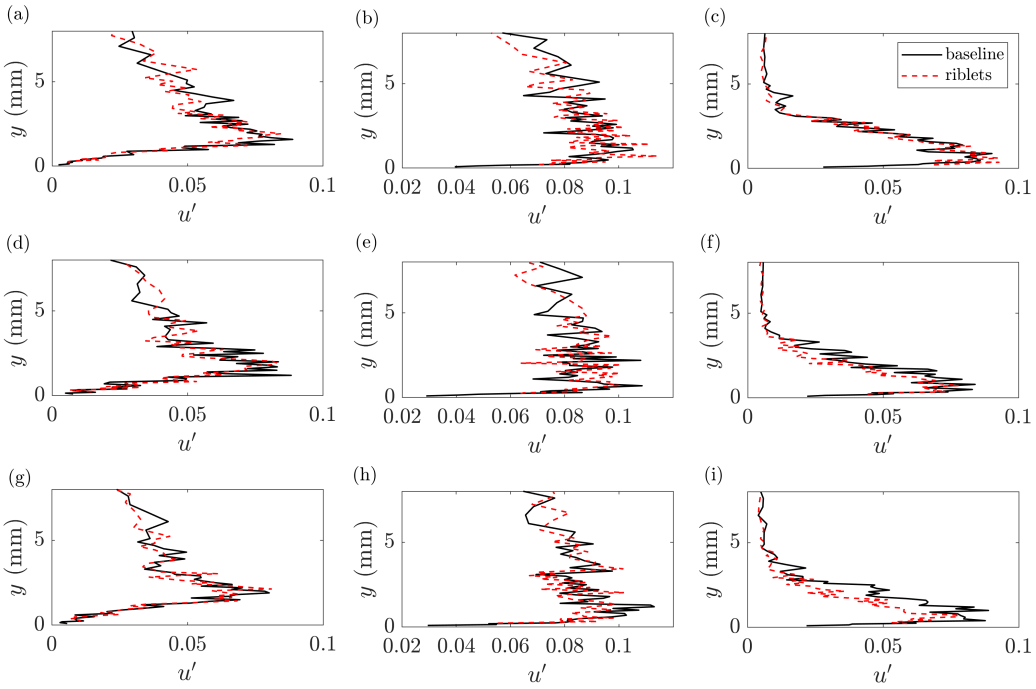

Figure 17: Presentation of u' as a function of y at (a), (b), (c): $x = X_{\text{ref}}$, for (a) $t' = t'_d$, (b) $t' = t'_e$, (c) $t' = t'_f$; (d), (e), (f): $x = X_{\text{ref}} + 40$ mm, for (d) $t' = t'_d$, (e) $t' = t'_e$, (f) $t' = t'_f$; (g), (h), (i): $x = X_{\text{ref}} + 80$ mm, for (g) $t' = t'_d$, (h) $t' = t'_e$, (i) $t' = t'_f$.

intensity and *secondary turbulence intensity* regions, respectively, remain unaffected by the riblets surfaces. Although not shown in this paper for brevity, examination for the turbulent spot contours under different x and t' reveals similarity in terms of the overall shape and dimension regardless the surface is of the baseline or riblets type. These observations for the frontal part and main body of a turbulent spot also correlate with the velocity perturbations shown in Figure 15.

Interestingly, some variations are also apparent at t'_f, which corresponds to the trailing edge of the turbulent spots. While the u' profile pertaining to the riblets is still largely similar to the baseline counterpart at X_{ref}, deviation begins to show at downstream locations, i.e. $X_{\text{ref}}+40$ mm and $X_{\text{ref}}+80$ mm where a reduction of the turbulence level is achieved by the riblets. After a joint-study with the velocity perturbations in Figure 15, two important phenomena can be attributed to the riblets:

1. A stronger sweeping event induced by the riblets at the turbulent spot's becalmed region could inject higher momentum to "re-laminarise" the local boundary layer. This re-laminarisation process, which commences at X_{ref} and is initially confined to the becalmed region only, can gradually be extended to the turbulent spot's trailing edge region as it continues to propagate downstream. This is manifested by the reduction of the turbulence intensity level of the boundary layer profiles near the spot's trailing edge at $X_{\text{ref}} + 40$ mm and $X_{\text{ref}} + 80$ mm.
2. The re-laminarisation process does not seem to be able to penetrate further upstream to the spot's leading edge region, where the *primary turbulence intensity* is located.

3.2.2. Implication to the turbulent boundary layer

Turbulent spots are considered as the *building blocks* of a turbulent boundary layer. Before a fully developed turbulent boundary layer is established, the transitional boundary layer contains multiple turbulent spots that are generated randomly in space and time. As each turbulent spot is convecting downstream, it will grow in length, height and width. These growths will facilitate merging of the neighbouring turbulent spots, resulting in intermittent laminar and turbulent events. A fully-developed turbulent boundary layer is only established when these turbulent spots are fully merged in space.

When the turbulent spots are convecting over a riblets surface, two mechanisms can collectively cause an eventual reduction of the turbulent velocity

profile, as well as the streamwise coherence level in the case of a fully developed turbulent boundary layer (Figure 6). First, the enhanced momentum achieved at each turbulent spot's becalmed region will mitigate the impact of turbulence merging with the neighbouring turbulent spots. Second, a process of "re-laminarisation" will be initiated, and gradually be extended towards the rear part of the turbulent spot. The combination of these two mechanisms will result in a turbulent boundary layer that contains lower turbulence intensity level (see Figure 6). However, it is important to point out that the convection velocities of the turbulent spot and turbulent eddies of a fully developed turbulent boundary layer (Figure 9) both remain unaffected by the riblets surface.

4. Conclusions

There are clear evidences that riblets can affect the way turbulence develops in a boundary layer, especially at the near wall region. For a turbulent boundary layer, the streamwise turbulence intensity can be reduced by the riblets, whilst the mean velocity increased. The riblets can also reduce the turbulent boundary layer thicknesses. The riblets are shown to reduce the skin friction coefficients of the turbulent boundary layer generated on a flat plate. The level of reduction is the greatest when the freestream velocity is low, but the effectiveness will reduce when the freestream velocity increases. This suggests that the riblets have some operational limitations where the effectiveness of skin friction reduction can only be achieved over a finite range of the ratio between the riblets height (h) and the boundary layer displacement thickness (δ^*). Based on the data acquired in this study, the non-dimensional height of the riblets should be $h/\delta^* > 0.2$ to become effective.

Whilst the convection velocities of the turbulent eddies remain unchanged between the riblets and smooth baseline surfaces, the riblets exhibit a streamwise coherence function decline, which suggests that they can alter the turbulence structure in the convective field (i.e. its longitudinal structure). However, the riblets may not change the fundamental turbulence re-generation mechanism significantly. The wall fluctuating pressure power spectral density (S_{qq}) shows that the riblets produce a reduction of the fluctuation level at the low and high frequency regions, but the mid-frequency range will experience an increase. These phenomena can be explained by the modification of momentum exchange between the inner layer and outer layer by the riblets. The process provides further modification of the turbulence structures

whose turbulent energy becomes more cinfined to the intermediate layer corresponding to the mid-frequency for the wall pressure spectra. On the other hand, the riblets can reduce the lateral coherence length scale (l_z) of the turbulence across a large frequency range, including at low frequency.

The product in the form of 10 $\log_{10}(l_z.\ S_{qq})$ could provide a hint of the trailing edge noise radiation subjected to the implementation of riblets on the wall surface. The results show that whilst the riblets can produce a lower value of 10 $\log_{10}(l_z.\ S_{qq})$ at the low and high frequency regions, they remain largely unchanged at the mid frequency range compared to the baseline due to the counter-balancing effect between the S_{qq} and l_z. In conclusion, riblets have a potential to achieve trailing edge self-noise reduction at the low and high frequency regions.

The study of turbulent spot convecting over the baseline and riblets surfaces in the spatial and temporal domains provide an opportunity to analyse the fundamental turbulence reduction mechanisms by the riblets implemented here. The results indicate that the riblets can reduce the turbulent velocity profile of a turbulent boundary layer by two factors. First, the enhanced momentum achieved at each turbulent spot's becalmed region will mitigate the impact of turbulence merging with the neighbouring turbulent spots during the process of transition, where the attenuation effect could remain active even at the fully-developed turbulent state. Second, the internal turbulence level at the rear part of turbulent spot can be reduced directly by the enhanced re-laminarisation process. These suggest that the reduced turbulence production by riblets is contributed mainly by the enhanced wall sweep, rather than the wall burst.

Acknowledgment

The authors would like to thank the PhD studentship sponsored by the Thomas Gerald Gray Charitable Trust in the United Kingdom.

References

[1] T. F. Brooks, S. D. Pope, M. A. Marcolini, Airfoil self-noise and prediction, NASA Reference Publication 1218, Retrieved from: https://ntrs.nasa.gov/archive/nasa/casi.ntrs.nasa.gov/19890016302.pdf, NASA Langley Research Center, Hampton (VA), (Accessed: 2020-04-08) (1989).

[2] I. A. Clark, W. N. Alexander, W. J. Devenport, S. A. L. Glegg, J. W. Jaworski, C. A. Daly, N. Peake, Bioinspired trailing-edge noise control, AIAA J 55 (2017) 740–754. doi:10.2514/1.J055243.

[3] A. Gonzalez, S. A. L. Glegg, N. Hari, M. Ottman, W. J. Devenport, Fundamental studies of the mechanisms of pressure shielding, in: 25^{th} AIAA/CEAS Aeroacoustics Conference, AIAA Paper 2019-2403, Delft, The Netherlands, 2019. doi:10.2514/6.2019-2403.

[4] M. S. Howe, Aerodynamic noise of a serrated trailing edge, J Fluid Struct 5 (1) (1991) 33–45. doi:10.1016/0889-9746(91)80010-B.

[5] B. Lyu, M. Azarpeyvand, S. Sinayoko, Prediction of noise from serrated trailing edges, J Fluid Mech 793 (2016) 556–588. doi:10.1017/jfm.2016.132.

[6] T. P. Chong, A. Vathylakis, On the aeroacoustic and flow structures developed on a flat plate with a serrated sawtooth trailing edge, J Sound Vib 354 (2015) 65–90. doi:10.1016/j.jsv.2015.05.019.

[7] F. Avallone, S. Pröbsting, D. Ragni, Three-dimensional flow field over a trailing-edge serration and implications on broadband noise, Phys Fluids 28 (2016) 117101. doi:10.1063/1.4966633.

[8] M. M. Scholz, T. P. Chong, E. Smith, New strategy on porous trailing edge for self-noise reductions, in: 27^{th} AIAA/CEAS Aeroacoustics Conference, AIAA Paper 2021-2109, Washington DC, USA, 2021. doi:10.2514/6.2021-2109.

[9] J. Jimenez, M. Uhlmann, A. Pinelli, G. Kawahara, Turbulent shear flows over active and passive porous walls, J Fluid Mech 442 (2001) 89–117. doi:10.1017/S0022112001004888.

[10] T. Geyer, E. Sarradj, C. Fritzsche, Measurement of the noise generation at the trailing edge of porous airfoils, Exp Fluids 48 (2010) 291–308. doi:10.1007/s00348-009-0739-x.

[11] S. Lee, L. Ayton, F. Bertagnolio, S. Moreau, T. P. Chong, P. Joseph, Turbulent boundary layer trailing-edge noise: Theory, computation, experiment, and application, Prog Aerosp Sci 126 (2021) 100737. doi:10.1016/j.paerosci.2021.100737.

[12] S. Walsh, Turbulent boundary layer drag reduction using riblets, in: 20^{th} Aerospace Sciences Meeting, AIAA, Orlando, USA, 1982. doi:10.2514/6.1982-169.

[13] D. W. Bechert, M. Bruse, W. Hage, J. G. T. van der Hoeven, G. Hoppe, Experiments on drag-reducing surfaces and their optimization with an adjustable geometry, J Fluid Mech 338 (1997) 59–87. doi:10.1017/S0022112096004673.

[14] S. J. Lee, S. H. Lee, Flow field analysis of a turbulent boundary layer over a riblet surface, Exp Fluids 30 (2001) 153–166. doi:10.1007/s003480000150.

[15] T. Guo, S. Zhong, T. Craft, Secondary flow in a laminar boundary layer developing over convergent-divergent riblets, Int J Heat Fluid Fl 84 (2020) 108598. doi:10.1016/j.ijheatfluidflow.2020.108598.

[16] E. Bacher, C. Smith, A combined visualization-anemometry study of the turbulent drag reducing mechanisms of triangular micro-groove surface modifications, in: Shear Flow Control Conference, AIAA, Boulder, USA, 1985. doi:10.2514/6.1985-548.

[17] J. Gallagher, A. Thomas, Turbulent boundary layer characteristics over streamwise grooves, in: 2^{nd} Applied Aerodynamics Conference, Seattle, USA, 1984. doi:10.2514/6.1984-2185.

[18] K.-S. Choi, Near-wall structure of a turbulent boundary layer with riblets, J Fluid Mech 208 (1989) 417–458. doi:10.1017/S0022112089002892.

[19] R. Garcia-Mayoral, J. Jimenez, Hydrodynamic stability and breakdown of the viscous regime over riblets, J Fluid Mech 678 (2011) 317–347. doi:10.1017/jfm.2011.114.

[20] T. P. Chong, S. Zhong, On the three-dimensional structure of turbulent spots, J Turbomach 127 (3) (2005) 545–551. doi:10.1115/1.1928286.

[21] C. Barbier, E. Jenner, B. D'Urso, Large drag reduction over superhydrophobic riblets, Fluid Dyn (2014). doi:10.48550/arXiv.1406.0787.

[22] F. Siegel, U. Klug, R. Kling, L. Z. Hannover, Extensive microstructuring of metals using picosecond pulses - ablation behavior and industrial relevance, J Laser Micro Nanoen 4 (2009) 104–110.

[23] B. Denkena, J. Köhler, B. Wang, Manufacturing of functional riblet structures by profile grinding, CIRP J Manuf Sci Technol 3 (1) (2010) 14–26. doi:https://doi.org/10.1016/j.cirpj.2010.08.001.

[24] D.-Y. Zhao, Z.-P. Huang, M.-J. Wang, T. Wang, Y. Jin, Vacuum casting replication of micro-riblets on shark skin for drag-reducing applications, J Mater Process Tech 212 (1) (2012) 198–202. doi:10.1016/j.jmatprotec.2011.09.002.

[25] L. Wen, J. C. Weaver, G. V. Lauder, Biomimetic shark skin: design, fabrication and hydrodynamic function, J Exp Biol 217 (2014) 1656–1666. doi:10.1242/jeb.097097.

[26] S. Saravi, K. Cheng, T. Chong, A. Vathylakis, Design of serrate-semicircular riblets with application to skin friction reduction on engineering surfaces, Int J Flow Control 6 (3) (2014) 83–92. doi:10.1260/1756-8250.6.3.83.

[27] M. Gruber, Airfoil noise reduction by edge treatments, PhD Thesis, University of Southampton. (2012). doi:http://eprints.soton.ac.uk/id/eprint/349012.

[28] A. P. Garcia Sagrado, Boundary layer and trailing edge noise sources, Ph.D. thesis, University of Cambridge (2008).

[29] D. W. Bechert, M. Bartenwerfer, The viscous flow on surfaces with longitudinal ribs, J Fluid Mech 206 (1989) 105–129. doi:10.1017/S0022112089002247.

[30] T. P. Chong, A. Juknevicius, Reconstruction of the deterministic turbulent boundary layer for the study of aerofoil self-noise mechanisms, Exp Fluids 63 (2022) 139. doi:10.1007/s00348-022-03486-7.

[31] I. Wygnanski, The effects of reynolds number and pressure gradient on the transitional spot in a laminar boundary layer, in: J. Jimenez (Ed.), The Role of Coherent Structures in Modelling Turbulence and Mixing, Springer Berlin Heidelberg, Berlin, Heidelberg, 1981, pp. 304–332.

[32] A. Glezer, Y. Katz, I. Wygnanski, On the breakdown of the wave packet trailing a turbulent spot in a laminar boundary layer, J Fluid Mech 198 (1989) 1–26. doi:10.1017/S0022112089000017.

[33] T. P. Chong, S. Zhong, On the momentum and thermal structures of turbulent spots in a favorable pressure gradient, J Turbomach 128 (4) (2006) 689–698. doi:10.1115/1.2218520.

[34] K. S. Yajnik, M. Acharya, Non-equilibrium effects in a turbulent boundary layer due to the destruction of large eddies, in: H. Fiedler (Ed.), Structure and Mechanisms of Turbulence I, Springer Berlin Heidelberg, Berlin, Heidelberg, 1978, pp. 249–260. doi:10.1007/3-540-08765-$6_2$4.

[35] S. Gravante, A. M. Naguib, C. E. Wark, H. M. Najib, Characterization of the pressure fluctuations under a fully developed turbulent boundary layer, AIAA J 36 (1998) 1808–1816. doi:10.2514/2.296.

[36] T. F. Brooks, T. H. Hodgson, Trailing edge noise prediction from measured surface pressures, J Sound Vib 78 (1) (1981) 69–117. doi:10.1016/S0022-460X(81)80158-7.

[37] G. Corcos, The structure of the turbulent pressure field in boundary-layer flows., J Fluid Mech 18 (1964) 353–378.

[38] R. K. Amiet, Noise due to turbulent flow past a trailing edge, J Sound Vib 47 (3) (1976) 387–393. doi:10.1016/0022-460X(76)90948-2.

[39] G. B. Schubauer, P. S. Klebanoff, Contributions on the mechanics of boundary-layer transition, Nasa reference publication 1289, retrieved from: https://ntrs.nasa.gov/api/citations/19930092285/downloads/19930092285.pdf, NASA Langley Research Center, Hampton (VA), (Accessed: 2021-07-05) (1956).

[40] J. P. Gostelow, N. Melwani, G. J. Walker, Effects of streamwise pressure gradient on turbulent spot development, J Turbomach 118 (4) (1996) 737–743. doi:10.1115/1.2840929.

[41] M. Gad-El-Hak, R. F. Blackwelderf, J. J. Riley, On the growth of turbulent regions in laminar boundary layers, J Fluid Mech 110 (1981) 73–95. doi:10.1017/S002211208100061X.